C. elegans Dicer acts with the RIG-I-like helicase DRH-1 and RDE-4 to cleave dsRNA

Claudia D. Consalvo[1], Adedeji M. Aderounmu[1,2], Helen M. Donelick[1,2], P. Joe Aruscavage[1], Debra M. Eckert[1], Peter S. Shen[1,*], Brenda L. Bass[1,3,*]

[1]Department of Biochemistry, University of Utah, Salt Lake City, UT 84112

[2]These authors contributed equally

[3]Lead Contact

*Correspondence: peter.shen@biochem.utah.edu (P.S.S) and bbass@biochem.utah.edu (B.L.B)

Abstract/Summary

Invertebrates use the endoribonuclease Dicer to cleave viral dsRNA during antiviral defense, while vertebrates use RIG-I-like Receptors (RLRs), which bind viral dsRNA to trigger an interferon response. While some invertebrate Dicers act alone during antiviral defense, *C. elegans* Dicer acts in a complex with a dsRNA binding protein called RDE-4, and an RLR ortholog called DRH-1. We used biochemical and structural techniques to provide mechanistic insight into how these proteins function together. We found RDE-4 is important for ATP-independent and ATP-dependent cleavage reactions, while helicase domains of both DCR-1 and DRH-1 contribute to ATP-dependent cleavage. DRH-1 plays the dominant role in ATP hydrolysis, and like mammalian RLRs, has an N-terminal domain that functions in autoinhibition. A cryo-EM structure indicates DRH-1 interacts with DCR-1's helicase domain, suggesting this interaction relieves autoinhibition. Our study unravels the mechanistic basis of the collaboration between two helicases from typically distinct innate immune defense pathways.

Introduction

RNA interference (RNAi) is a conserved pathway that likely had an ancestral role in defending genomes against selfish elements and viruses[1–3]. Modern day invertebrates still rely on RNAi for viral defense, while in most vertebrates, the interferon pathway is the primary means of fighting a viral infection. However, a role for RNAi in vertebrate innate immunity has not been ruled out[4,5], and as in all animals, vertebrates encode the machinery for RNAi, where it functions in regulation of endogenous gene expression via small RNAs[6].

A key player in RNAi is Dicer, a multidomain, ribonuclease (RNase) III family member[7] (Figure 1A) that cleaves viral or endogenous dsRNA into microRNAs (miRNAs) or small interfering RNAs (siRNA)[6]. The tandem RNase III domains of Dicer (RNaseIIIa and RNaseIIIb) each cleave one strand to produce a staggered cleavage product, yielding a small dsRNA with 3' overhangs (3'ovr), and strands of ~21-27 nucleotides (nts), each with a 5' phosphate and 3' hydroxyl. Animal Dicers have an N-terminal helicase domain (Figure 1A), and whether the helicase domain functions to hydrolyze ATP coincides with antiviral functions. For example, in *Drosophila melanogaster* there are two Dicer enzymes: Dicer-1 (dmDcr1) and Dicer-2 (dmDcr2). dmDcr1 has a degenerate helicase domain, and in an ATP-independent manner, cleaves miRNA precursors to generate mature miRNA[8,9]. By contrast, ATP hydrolysis by the helicase domain of dmDcr2 fuels translocation and processive cleavage of viral or endogenous dsRNA into siRNA[10,11], and mutations in this domain increase susceptibility to viral load[12,13]. dmDcr2 cleaves dsRNA with blunt (BLT) termini more efficiently than those with 3'ovrs, and it is speculated that this allows discrimination between self and nonself dsRNA[10,11,14,15]. Despite having a conserved helicase domain, a requirement for ATP has not been reported for vertebrate Dicers, including human Dicer (hsDcr-1); in fact, the helicase domain of hsDcr-1 inhibits cleavage activity[16].

While Dicer binds and cleaves viral dsRNA to trigger antiviral RNAi in invertebrates, the recognition of viral dsRNA during a vertebrate interferon response is performed by RIG-I-like

Receptors (RLRs)[17]. Despite differences in their domain organization and functions, Dicer and RLRs share a conserved DExD/H-box helicase domain (Figure 1A)[18]. The best characterized RLRs, RIG-I and MDA5, use their ATP-dependent helicase domains to bind viral dsRNA and stimulate a cascade of events that induces the Type I Interferon response[19–21]. Like dmDcr2, RIG-I distinguishes between self from non-self using dsRNA termini by recognizing BLT dsRNA; in contrast, MDA5 prefers long dsRNA[22,23]. Interestingly, in some cases Dicer and the interferon response have antagonistic interactions, for example, the RLR LGP2 inhibits human Dicer's ability to cleave dsRNA[24,25].

The conservation of Dicer's helicase domain with that of RLRs suggests this domain functioned in antiviral defense in a common ancestor, and it is fascinating to imagine the host-virus arms race that led to the distinctly different innate immune pathways of extant vertebrates and invertebrates. *C. elegans* is of keen interest in this regard because its single encoded Dicer functions in complex with an RLR homolog to meditate an antiviral RNAi response[26–28]. The antiviral complex in *C. elegans* includes Dicer (DCR-1), the RIG-I ortholog called Dicer-Related Helicase-1 (DRH-1), and a dsRNA binding protein called RNAi deficient-4 (RDE-4; Figure 1A)[26,29]. Like RIG-I and MDA5[17,28], DRH-1 has an N-terminal domain (NTD), a central helicase domain, and a C-terminal regulatory domain (CTD; Figure 1A). RDE-4 is a dsRNA binding protein (dsRBP) that contains three dsRNA binding motifs and has a high affinity for binding long dsRNA[30,31].

RNAi was first discovered in *C. elegans*[32], but efforts to characterize DCR-1 have been hampered by challenges to purify it in a recombinant form. Here we overcome this bottleneck by co-expressing and purifying the antiviral complex comprising DCR-1, DRH-1, and RDE-4. The complex exhibits some features previously observed in vitro for purified dmDcr2, such as cleavage and ATP hydrolysis activity that depends on dsRNA termini[11,15,33]. However, comparison of the activity of the wildtype antiviral complex with complexes containing point mutations in the helicase domain of DCR-1 or DRH-1 demonstrate that ATP hydrolysis activity

comes primarily from DRH-1. While Dicer enzymes are commonly found to have dsRBPs that bind their helicase domain to facilitate substrate specificity and regulate cleavage[34], RDE-4 plays a critical role in all activities of the *C. elegans* antiviral complex, and dsRNA binding, cleavage and ATP hydrolysis are all greatly compromised in its absence. Finally, we supplement our biochemical studies with cryo-EM structure determination, providing mechanistic insight into how these three proteins cooperate in antiviral defense.

Results

Purification of the *C. elegans* antiviral complex, DCR-1•DRH-1•RDE-4.

We co-expressed DCR-1, DRH-1, and RDE-4 in Sf9 cells from a single baculovirus expression plasmid[35]. The construct included a One-STrEP-FLAG tag on the N-terminus of DRH-1, allowing affinity purification using Strep-Tactin, and subsequently the complex was purified to ≥90% homogeneity by size-exclusion chromatography (SEC). Analysis of the complex by SDS-PAGE showed three major bands (Figure S1A), which were validated as DCR-1, DRH-1 and RDE-4, using mass spectrometry and western blot analyses (Figure S1B and S1C). Using this approach, we also purified three variants of the complex containing point mutations in the Walker A motif of DCR-1 (G36R), DRH-1 (K320A) or lacking RDE-4 (Figure 1B and S1D). Sedimentation velocity analytical ultracentrifugation (SV-AUC) analyses indicated DCR-1•DRH-1•RDE-4 and DCR-1•DRH-1 complexes have a 1:1:1 and 1:1 stoichiometry, respectively (Figure S1E-G).

The catalytically active DCR-1•DRH-1•RDE-4 complex cleaves dsRNA in a terminus and ATP-dependent manner.

Like *C. elegans*, *D. melanogaster* uses RNAi for antiviral defense[12,13], and the key enzyme in this pathway, dmDcr2, is biochemically well characterized[11,15,33]. Although the

antiviral complex contains two proteins in addition to DCR-1, as a first step in characterizing its biochemical activity, we tested whether the *C. elegans* antiviral complex had activities exhibited by dmDcr2 alone, such as dependencies on ATP and dsRNA termini. Using the *C. elegans* antiviral complex, we conducted single-turnover cleavage assays using a 106 base-pair (bp) dsRNA (106-dsRNA) with BLT or 3'ovr termini either with or without ATP (Figure 1C and 1D). The sense strand was 5' ^{32}P-end-labeled and contained a 2',3' cyclic phosphate at the opposite end to minimize cleavage from that end (Figure S2), allowing us to focus on the first cleavage event from the radiolabeled terminus (Figures 1C,1D).

In the absence of ATP, the complex inefficiently cleaved BLT and 3'ovr dsRNA at similar rates (Figure 1C and dashed lines in 1E), but the radiolabeled siRNA product was 26nt using a BLT dsRNA, and 24nt using 3'ovr dsRNA. With ATP, the efficiency of BLT dsRNA cleavage was dramatically enhanced, and gave rise to an additional ATP-dependent siRNA product of 27nt, while the time course of 3'ovr dsRNA cleavage was relatively unchanged (Figure 1D and 1E). The 26nt and 27nt siRNAs produced from a BLT dsRNA terminus were consistent with previous experiments using *C. elegans* embryo extracts[10,36]. However, the 24nt siRNA band with 3'ovr dsRNA was one nucleotide longer than previously reported[10], possibly due to a protein cofactor that is not present in our in vitro system.

Differential processing of dsRNA based on termini is reminiscent of dmDcr2, which preferentially cleaves BLT dsRNA in the presence of ATP, even without other factors[11]. However, there are notable differences between the DCR-1•DRH-1•RDE-4 complex and dmDcr2. dmDcr2 cannot cleave BLT dsRNA without ATP[14], but the DCR-1•DRH-1•RDE-4 complex readily cleaved dsRNA in the absence of ATP (Figures 1C and S3A). In addition, with ATP, at least in vitro, dmDcr2 threads dsRNA through the helicase domain, and as dsRNA passes the RNase III active sites, it is cleaved to yield heterogeneous-sized siRNA products[11]. In contrast, we observed that the antiviral complex produced siRNAs of discrete lengths.

Possibly, the presence of DRH-1 and RDE-4 allow a more precise measuring of siRNA products.

DRH-1 is an RLR homolog, and RIG-I primarily recognizes BLT dsRNA with a 5'-triphosphate (5'ppp). By contrast, with the antiviral complex we saw little difference in cleavage (Figure S3B and S3C) or ATP hydrolysis (Figure S3D and S3E) when comparing BLT 106-dsRNA with a 5'p or 5'ppp. Thus, for the antiviral complex, a BLT terminus is more important for recognition than the phosphorylation state, at least under these conditions. This is also the case for dmDcr2, where 5' phosphorylation state does not impact its ability to cleave dsRNA[11].

ATP-dependent cleavage is mediated by DCR-1 and DRH-1 helicase domains, whereas RDE-4 is needed for both ATP-independent and ATP-dependent cleavage.

To understand contributions of each protein to terminus-dependent processing of dsRNA, we compared cleavage reactions of wildtype antiviral complex to the three variants, in the presence or absence of ATP, or with the nonhydrolyzable analog ATPγS (Figure 2A and Figure 2B). Cleavage efficiency using the wildtype complex (Figure 2A and 2B, lanes 1-3) increased with ATP, but not with ATPγS, indicating that optimal cleavage requires ATP hydrolysis. The 27nt siRNA produced from BLT dsRNA was observed with ATP, but not with ATPγS (Figure 2A, lanes 2-3), emphasizing that this product is completely dependent on ATP hydrolysis. Again, in the presence of ATP, the reaction with BLT dsRNA (k_{obs}, 0.14 min^{-1}) was more efficient compared to that with 3'ovr dsRNA (k_{obs}, 0.006 min^{-1}; Figure 2C and Table 1).

In the presence of ATP, antiviral complexes with a point mutation in the Walker A motif (Figure 1B) of the helicase domain of DCR-1 (G36R) or DRH-1 (K320A), reduced cleavage efficiency of BLT dsRNA, demonstrating that ATP hydrolysis by both helicase domains is important for optimal cleavage from this terminus (Figures 2A, compare lanes 3, 6 and 9, and 2C, compare solid black, green and blue curves; Table 1, S4A, and S4B). The complex containing the DCR-1 G36R mutation showed a loss of the 27nt siRNA band (Figures 2A,

compare lanes 3 and 6, and S4A). This is consistent with work done using extracts from *C. elegans* containing a mutation in DCR-1's helicase domain[10], thereby confirming a role for DCR-1's Walker A motif in production of this slightly longer siRNA. By contrast, the DRH-1 K320A mutation reduced overall cleavage (Figure 2C; Table 1), but the siRNA doublet was apparent (Figure 2A, compare lane 3 with 9, S4B). For the Walker A mutations in either DCR-1 or DRH-1, we observed no effect on cleavage of BLT or 3'ovr dsRNA in the absence of ATP or with ATPγS (Figure 2A and 2B, compare lanes 1-2 with 4-5 and 7-8). With 3'ovr dsRNA, we observed little effect of the Walker A mutations on cleavage, regardless of the presence or absence of nucleotide (Figure 2B, compare lanes 1-9 and Figure 2C dashed curves; Table 1, S4A and S4B).

The most dramatic effects among the three variants were observed with the DCR-1•DRH-1 complex that lacked the RDE-4 protein. Cleavage of BLT dsRNA was only observed with ATP, and this occurred with low efficiency (Figure 2A, compare lanes 1-3 with lanes 10-12; Figure 2C, compare solid black and purple curves; S4C). Cleavage with this complex was undetectable with 3'ovr dsRNA regardless of whether nucleotide was present (Figure 2B, compare lanes 1-3 with 10-12; S4C). While RDE-4 was clearly necessary for 3'ovr cleavage, the small amount of siRNA of the correct size observed with BLT dsRNA and ATP indicated measuring and cleavage by the RNase III domains were functional in the DCR-1•DRH-1 complex.

Taken together, these studies indicate RDE-4 plays a significant role in promoting all cleavage reactions by the DCR-1•DRH-1•RDE-4 complex, whereas the helicase domains of DCR-1 and DRH-1 only impact ATP hydrolysis-dependent cleavage, and this effect was most observable with BLT dsRNA (Figure 2). The loss in cleavage efficiency in the presence of ATP was greater with the DCR-1•DRH-1^{K320A}•RDE-4 complex (BLT, k_{obs}, 0.013 min^{-1}) than the DCR-1^{G36R}•DRH-1•RDE-4 complex (BLT, k_{obs}, 0.05 min^{-1}; Table 1), albeit the loss of the 27nt ATP

dependent band was only observed with the latter, suggesting that DCR-1 is involved in an ATP hydrolysis-dependent measuring step.

DRH-1 is essential for in vitro ATP hydrolysis in the *C. elegans* antiviral complex.

Dicer and RLRs belong to the Super Family 2 nucleic acid-dependent ATPases (SF2 helicases), which require dsRNA binding for optimal enzymatic activity[18]. As expected, DCR-1•DRH-1•RDE-4 showed negligible amounts of ATP hydrolysis in the absence of dsRNA or in the presence of single-stranded RNA (Figure S4D and S4E) but had robust ATP hydrolysis activity in the presence of dsRNA (Figure 2D and 2H). Our cleavage assays indicated that ATP hydrolysis by both helicases affected cleavage (Figure 2A and 2C). In order to gain more insight into the ATP-dependent roles of DCR-1 and DRH-1, we directly monitored conversion of ATP to ADP over time, in the presence of BLT or 3'ovr dsRNA, for the wildtype antiviral complex and all variants (Figure 2D and 2H; Table 1). Reactions were performed with excess dsRNA to focus on differences in the catalytic step, rather than differences in affinity for dsRNA, and products were separated by Thin-Layer Chromatography (TLC). Again, similarities to dmDcr2 were observed; for example, the wildtype complex was more efficient in ATP hydrolysis in the presence of BLT dsRNA (BLT, k_{obs}, 0.11 min^{-1}) compared to 3'ovr dsRNA (3'ovr, k_{obs}, 0.03 min^{-1}; Table 1 and Figures 2D and 2H). Unexpectedly, while reaction with the complex containing DCR-1^{G36R} reduced the rate of ATP hydrolysis for both dsRNA termini (Figure 2E and 2H), ATP hydrolysis was completely eliminated with complexes containing DRH-1^{K320A} (Figure 2F and 2H). The DCR-1•DRH-1 variant that lacked RDE-4 was also severely compromised in the production of ADP over time (Figure 2G and 2H).

Proteins in the antiviral complex contribute to high affinity binding to dsRNA.

We used gel-shift assays to compare dsRNA binding by the wildtype antiviral complex with the three variants. The wildtype antiviral complex and all variants bound 106-dsRNA tightly,

showing dissociation constants (K_ds) ranging from 0.3 to 29 nM (Figures 3 and S5; Tables 1 and S1), with only small differences in the presence or absence of ATP or with different termini.

Despite the large mass of the antiviral complex (386 kDa), distinct, but sometimes diffuse, gel shifts were observed. The DCR-1•DRH-1•RDE-4 wildtype complex showed a similar gel-shift pattern for BLT and 3'ovr dsRNA (Figures 3A and S5A), with two prominent bands in the absence of ATP that became diffuse in the presence of ATP. These diffuse bands were not observed when ATPγS was substituted for ATP (Figure S6A), suggesting ATP hydrolysis promotes the diffuse appearance. We confirmed that ATP hydrolysis occurs at 4°C, the temperature used for gel-shift assays (data not shown). These general trends were observed for gel-shift patterns using complexes containing point mutations in the helicase domain of DCR-1 or DRH-1 (Figures 3B, 3C, S5B, and S5C), but consistent with its dominant role in ATP hydrolysis, the addition of ATP to DCR-1•DRH-1^{K320A}•RDE-4 did not lead to more diffuse bands (Figures 3C and S5C). The two-band gel shifts observed with wildtype and helicase mutant complexes were not observed with the DCR-1•DRH-1 complex that lacked RDE-4 (Figures 3D and S5D). This complex showed a diffuse gel-shift, suggesting the presence of RDE-4 is required for the two discrete bands observed with complexes that contained all three proteins.

Quantification of multiple gel-shift experiments allowed determination of dissociation constants (Tables 1 and S1). Binding affinities under the different conditions were similar for DCR-1•DRH-1•RDE-4 and the DCR-1^{G36R}•DRH-1•RDE-4 complex, while affinities decreased 2 to 3-fold for the DCR-1•DRH-1^{K320A}•RDE-4 complex. The DCR-1•DRH-1 complex that lacked RDE-4, while still binding tightly, was 7-30 fold weaker than the wildtype complex, depending on the condition. For all complexes, addition of ATP decreased binding affinity. For complexes that contained all three proteins, BLT dsRNA was bound slightly tighter than 3'ovr dsRNA in the presence of ATP, but terminus dependence was not observed without ATP. The complex lacking RDE-4 showed the greatest differences in ATP and terminus dependence. Adding ATPγS instead of ATP decreased binding affinity further than ATP did, suggesting that ATP

binding, not hydrolysis, is the primary force driving the loss of binding affinity (Figure S6A, S6B, and S6G; Table S1).

Studies of hsDcr-1 and dmDcr2 indicate ATP-independent cleavage is mediated by the Platform•PAZ domain, rather than the helicase domain[11,15,37,38]. Our observation that ATP-independent cleavage is lost when dsRNA termini are blocked with 2', 3'-cyclic phosphates (Figure S2), suggests this modification precludes interaction of dsRNA with the Platform•PAZ domain of DCR-1. To delineate contributions of binding to the Platform•PAZ domain of DCR-1, we performed binding assays of DCR-1•DRH-1•RDE-4 and a 106-mer BLT dsRNA with 2', 3'-cyclic phosphates on both ends. With ATP, binding of DCR-1•DRH-1•RDE-4 or DCR-1•DRH-1 to cyclic phosphate-blocked BLT dsRNA was similar to binding to BLT dsRNA without the cyclic phosphate block (Figure S6C, S6D, S6H), and K_d values were nearly identical (Table S1). This is consistent with the idea that in the presence of ATP, binding is predominantly to the helicase domain of DCR-1 or DRH-1, similar to what is observed in dmDcr2[39]. In the absence of ATP, DCR-1•DRH-1•RDE-4 binds both types of BLT dsRNA with similar affinities (Figure S6E; compare Tables 1 and S1), but DCR-1•DRH-1 binds 2.5-fold better to BLT dsRNA than it does to cyclic blocked BLT dsRNA (Figure S6F, S6H; compare Tables 1 and S1). This suggests that the 2', 3'-cyclic phosphate blocks terminus binding to the PAZ/Platform domain but the presence of RDE-4 in the wildtype complex mutes this effect.

Cryo-EM analyses give insight into ATP-independent and ATP-dependent cleavage mechanisms.

To better understand how each protein in the *C. elegans* antiviral complex contributes to dsRNA processing, we used cryo-EM to determine structures of DCR-1•DRH-1•RDE-4 in the presence of dsRNA substrates, with or without nucleotide. We obtained a 6.1 Å reconstruction of DCR-1•DRH-1•RDE-4 bound to a 52-BLT dsRNA (Figures 4A and S7). Our density map revealed the canonical "L shape" of Dicer[11,40–43], which enabled rigid-body fitting of a human

Dicer model. The reconstruction contained extra density at the Hel2i subdomain of the DCR-1 helicase domain, a known binding site of dsRBPs, such as human TRBP and *Drosophila* R2D2[40,41]. Indeed, when fitting the human Dicer•TRBP model[40] into our density, the extra density was accommodated by the third dsRNA binding motif (dsRBM) of TRBP, and by analogy, we propose this density corresponds to a single dsRBM of RDE-4 (Figure 4A). In our 3D reconstructions, we also observed additional density interacting with Dicer's helicase domain near the Hel1 subdomain. In this density we were able to fit AlphaFold2 models of DRH-1 NTD and helicase domains as separate rigid bodies (Figure 4A)[44,45]. These fits showed the NTD of DRH-1 directly interacting with DCR-1's helicase domain, with DRH-1's helicase and CTD domains extended away from DCR-1 and bound to the end of the 52-BLT dsRNA (Figure 4A).

In a separate reconstruction, we solved DCR-1•DRH-1•RDE-4 bound to 42-BLT dsRNA to 7.6 Å (Figures 4B and S8). This structure was similar to our 6.1 Å reconstruction, with the exception of additional dsRNA density bound to DCR-1 (compare Figure 4A and 4B). We fit the human Dicer•TRBP•pre-miRNA Class 1 structure[40] as a rigid body into our complex and found that there is a slight difference in the position of the dsRNA; however, like the human Dicer structure, our density indicates that the 42-BLT dsRNA is positioned away from the RNase III active sites. This state likely represents a pre-dicing conformation, similar to many other studies that show the importance of the PAZ domain in positioning pre-miRNA for ATP independent cleavage[40,46,47]. In both of our reconstructions, we observed DRH-1 bound to dsRNA termini (Figure 4A and 4B); however, it was still unclear how DRH-1 utilizes ATP to promote ATP-dependent cleavage. We speculated that the dsRNA bound to DRH-1 was trapped in an initial dsRNA binding state, because our reconstructions thus far excluded ATP and were performed in the absence of nucleotide or with ATPγS.

To understand how ATP hydrolysis was coupled to cleavage, we prepared cryo-EM specimens of DCR-1•DRH-1•RDE-4 in the presence of ATP, and added Ca^{2+} in addition to Mg^{2+} to inhibit dsRNA cleavage (see Materials and methods). Under these conditions, we obtained a

2.9 Å reconstruction of the helicase and CTD domains of DRH-1 positioned internally on the dsRNA (Figures 4C and S9), suggesting that DRH-1 hydrolyzes ATP to translocate along dsRNA. Density for DCR-1, RDE-4, and the NTD of DRH-1 was not observed in this reconstruction, presumably due to increased flexibility in the presence of ATP.

The reconstruction showed DRH-1 in a closed conformation where Hel1, Hel2, Hel2i, and the CTD were wrapped around the dsRNA to make a network of contacts with both strands (Figure 4C and 4D). The N-terminal RecA fold (Hel1) was positioned next to the second RecA fold (Hel2). The ATP-binding pocket at the interface of these domains contained density for ADP and Mg^{2+}, stabilized by contacts from well conserved helicase motifs including Q, I, Ia, II, III, Va, and VI (Figure 4E and S10). Direct binding to ADP-Mg^{2+} involves residues from motif Q (Q297), motif I (K320 and T321), motif Ia (Q357), and motif II (D430) (Figures 4E and S10). Motif Q recognizes adenine and mediates binding specificity to ATP as in other SF1 and SF2 helicases with R294's sidechain forming stacking interactions with the adenine base, in addition to the hydrogen bonds between Q297 and adenine N_6 and N_7 (Figure 4E)[48–50]. R808 from Motif VI is positioned to make contact with the beta phosphate of the ADP molecule. In the Hel2 subdomain, a conserved loop between motifs IVa and IVb was inserted into the major groove of the dsRNA (Figures 4F and S10), with a concomitant widening of the groove (Figures 4F, S11A, and S11B). The analogous loop of MDA5 interacts with a widened major groove and is crucial for dsRNA-dependent ATP hydrolysis by MDA5[51,52]. In RIG-I, motif IVa is disordered to accommodate a 5'ppp or m7G moiety, but is observed with dsRNA containing a 5'OH, or when RIG-I is internally bound to dsRNA[53,54]. Deletion of this loop in RIG-I reduces ATP hydrolysis and inactivates signaling[53]. Furthermore, RIG-I's loop contains two threonine residues (T667 and T671) that when phosphorylated impair RIG-I translocation and signaling[55,56] (Figure S10, see arrows pointing down). Interestingly, DRH-1's Hel2 loop has two serines (S741 and S745) that align with RIG-I's threonines (Figure S10), raising the possibility that DRH-1 might also be regulated by phosphorylation state.

The Hel2i subdomain, an alpha helical insertion domain unique to RLRs and metazoan Dicers, is comprised of five alpha helices and is inserted between Hel2 and the CTD. The pincer subdomain forms the canonical V-shape that acts as a bridge connecting Hel1, Hel2, and the CTD. In the CTD, we observed a patch of lysine residues (K987, K988, and K990) that make extensive contact with phosphates in the RNA backbone (Figure 4D and 4G). Interestingly, Guo *et al.* demonstrated that a *C. elegans drh-1* null mutant animal carrying an extrachromosomal array encoding DRH-1 with point mutations K988A, W987A, and K990A, failed to rescue RNAi[28], which suggests these residues are key in maintaining contact with dsRNA. K988 and W989 are conserved in RLRs, indicating these are important residues in the CTD (Figure S10). We also found that the CTD contains a zinc structural ion that is conserved with RLRs (Figures S10, see arrows pointing up, and S11C). Overall, the tertiary structure of DRH-1 was well conserved with RLRs (Figure S11D). The RMSD of DRH-1 to an internally bound RIG-I (PDB 7TO2) was 1.706 Å, while to MDA5 (PDB 4GL2) it was 1.708 Å.

The NTD of DRH-1 is autoinhibitory.

When full-length DRH-1 was purified by itself, we found that it could not hydrolyze ATP (Figure 5A, DRH-1). Since our structural studies suggested that DRH-1 translocated along dsRNA, we considered the possibility that interaction of its NTD with DCR-1's helicase domain released DRH-1 from an autoinhibited state. This was an attractive model by analogy to RIG-I, which contains two N-terminal caspase activation and recruitment domains (CARDs) (Figure 1A) involved in autoinhibition. In the absence of dsRNA, the second CARD (CARD2) interacts with RIG-I's Hel2i domain to stabilize an autoinhibited conformation and prevent signaling of an interferon response[19,57]. In the presence of its optimal substrate, a 5’ppp BLT dsRNA, RIG-I's CTD and helicase domains bind the dsRNA terminus, promoting a conformational change that disrupts the CARD2 interaction and autoinhibition. This allows RIG-I to translocate along dsRNA, form oligomers, and signal an interferon response[56,58]. In the absence of DCR-1 and

RDE-4, full-length DRH-1 cannot hydrolyze ATP with or without dsRNA (Figure 5A; data not shown), however, we found that deletion of its NTD (ΔNTD DRH-1), allowed ATP hydrolysis in a terminus-dependent manner (Figure 5A and 5B). Based on these results and our structural data (Figure 4A and 4B), we propose that the NTD of DRH-1, like RIG-I's CARD domains, interacts with its own helicase domain to promote an autoinhibited state. While binding to dsRNA relieves autoinhibition for RIG-I, for DRH-I we propose it is the binding of its NTD to DCR-1's helicase domain, instead of its own helicase domain, that relieves DRH-1's autoinhibited state (Figure 4). Moreover, ΔNTD DRH-1 hydrolyzes ATP more efficiently in the presence of blunt dsRNA as opposed to 3'ovr dsRNA, suggesting that, like RIG-I, DRH-1 recognizes dsRNA termini (Figure 5A and 5B).

DCR-1•DRH-1•RDE-4 processively cleaves BLT dsRNA.

Given that DCR-1•DRH-1•RDE-4 cleaves BLT dsRNA in an ATP-dependent manner (Figure 1C – 1E), and our data suggest DRH-1 hydrolyzes ATP for translocation (Figures 2H and 4C), we wondered if translocation was coupled to processive cleavage. To test this, we performed trap experiments where DCR-1•DRH-1•RDE-4 was allowed to cleave ^{32}P-internally labeled BLT dsRNA for a short time, followed by addition of excess nonradiolabeled (cold) dsRNA. When cold dsRNA was added second, we saw a small continued accumulation of siRNA over time, albeit the increase was slight (Figure 5C and 5D), consistent with the idea that DCR-1•DRH-1•RDE-4 remained associated with dsRNA during successive cleavage events. Additional support for the role of DRH-1 in processive cleavage came from single turnover cleavage assays using ^{32}P-internally-labeled BLT dsRNA to allow visualization of the initial cleavage event from the terminus (e.g., Figure 1), as well as siRNAs from internal cleavage (Figure 5E). For WT complex in the presence of ATP, the 26nt and 27nt siRNA bands that correspond to the initial cleavage from the terminus were observed, as well as a cluster of smaller siRNAs (~21-23nts). Based on prior studies[10], the 23nt species is predicted to be

comprised of siRNAs produced from the initial cleavage from the opposite end, as well as internal cleavage, while the 21nt and 22nt species derive exclusively from internal cleavage (Figure 5E, see red line). Importantly, the DCR-1•DRH-1^{K320A}•RDE-4 complex showed the greatest loss in the production of internal siRNAs (Figure 5E). A similar loss of internal siRNA was observed in the presence of ^{32}P-internally labeled 3'ovr dsRNA only when DRH-1's helicase is mutated (Figure 5E, blue line 22-23nts). Since DRH-1 is required for ATP hydrolysis (Figure 2F and 2H), it is possible that DRH-1 is needed to allow DCR-1 to processively cleave dsRNA. This observation is supported by Coffman *et. al*, who showed that *C. elegans* strains containing *drh-1* mutations accumulated siRNAs corresponding to terminal regions of the Orsay virus genome, but lost viral siRNAs mapping to internal regions[59].

Discussion

Here we report the first biochemical characterization of *C. elegans* Dicer in a recombinant form. Key to the successful purification of DCR-1 was its co-expression and purification with two proteins known to associate with DCR-1: the RIG-I ortholog DRH-1, and the dsRBP RDE-4[26,29]. Prior studies show that all three proteins are required to cleave viral dsRNA into viral siRNAs during the *C. elegans* antiviral response[26–29,60]. Our structural studies reveal physical interactions between the three proteins, and combined with our biochemical assays, provide insight into the mechanism of a molecular motor that requires two helicases and a dsRBP. By comparing the wildtype antiviral complex to complexes with a Walker A mutation in the helicase domain of DCR-1 or DRH-1, or a complex lacking RDE-4, we gained insight into the contributions of the three proteins to the processing of dsRNA.

Relationship to previously characterized Dicer activities

Vertebrates primarily rely on RLRs and the interferon response for antiviral defense, and their Dicer enzymes have not been observed to require ATP. By contrast, invertebrate antiviral defense occurs through the RNAi pathway using Dicer enzymes that are ATP dependent. The most biochemically well characterized invertebrate antiviral Dicer is dmDcr2, which cleaves dsRNA in an ATP- and dsRNA terminus-dependent manner in vitro, without accessory factors; studies in flies indicate these same properties exist *in vivo*[13]. We find that the *C. elegans* antiviral complex is also ATP and terminus dependent. Like dmDcr2, the *C. elegans* antiviral complex cleaves BLT dsRNA more efficiently than 3'ovr dsRNA (Figure 1E), and with 106-dsRNA (1nM) the single turnover cleavage rates for purified dmDcr2 (30nM) with ATP (BLT, k_{obs}, 0.19 min^{-1}; 3'ovr, k_{obs}, 0.01 min^{-1})[14] are almost identical to the rates observed with the *C. elegans* complex (25nM) (BLT, k_{obs}, 0.14 min^{-1}, 3'ovr, k_{obs}, 0.006 min^{-1}, Table 1). We find it remarkable that the enzymatic properties for dsRNA cleavage are so similar, given that dmDcr2 orchestrates cleavage with a single protein, while two helicases and a dsRNA binding protein cooperate in the *C. elegans* reaction.

There are also differences between the two antiviral activities. Like dmDcr2, for the *C. elegans* antiviral complex, ATP hydrolysis is faster with BLT dsRNA (k_{obs}=0.11 min^{-1}) compared to 3'ovr dsRNA (0.002 min-1)(Table 1). However, a mutation in the Walker A motif of DCR-1 reduces both of these values, but a similar mutation in DRH-1 completely eliminates detectable hydrolysis, indicating DRH-1 is the primary driver of ATP hydrolysis in the *C. elegan*s antiviral complex. Indeed, DRH-1 alone hydrolyzes ATP with BLT dsRNA at almost the same rate as the complex (k_{obs}, 0.08 min^{-1}) in a terminus-dependent manner (Figure 5A), emphasizing the key role it plays in the antiviral complex. That said, we observed a one nucleotide longer siRNA that was dependent on ATP hydrolysis by DCR-1 (Figure 2A), indicating that DCR-1 contributes to the ATP-dependence of the reaction. Also, although we see ATP-dependent cleavage, the cleavage pattern is remarkably different than dmDcr2. In the presence of ATP, dmDcr2

produces heterogeneous sized siRNA products whereas the *C. elegans* antiviral complex produces discrete siRNA bands. These discrete siRNA bands are more similar to human Dicer, although human Dicer does not cleave dsRNA in an ATP-dependent manner[37,46].

Another difference is that, while dmDcr2 readily cleaves 3'ovr dsRNA in the absence of ATP, it has a strict requirement for ATP in processing BLT dsRNA. By contrast we observe ATP independent cleavage for both 3'ovr and BLT dsRNA with the *C. elegans* complex, and our studies indicate RDE-4 is important for this ATP-independent cleavage. In complexes lacking RDE-4, cleavage is only detected in the presence of ATP and BLT dsRNA, and even this reaction is barely detectable (Figure 2A-C). Our biochemical studies indicate that RDE-4 is important for dsRNA binding, and this is not surprising since it consists of three dsRBMs. The DCR-1•DRH-1 complex, which lacks RDE-4, shows approximately 10-fold weaker binding for BLT dsRNA (5.18 nM) and 32-fold weaker binding (28.64nM) for 3’ovr dsRNA, suggesting that RDE-4 dampens the difference in affinity for different termini conferred by DCR-1 and/or DRH-1 (Table 1). In this regard RDE-4 is similar to the dsRBP Loquacious-PD (Loqs-PD), an accessory factor of dmDcr2 that is required for processing endogenous, but not viral, dsRNA. Loqs-PD decreases dmDcr2's terminus dependence, and for example, while BLT dsRNA is cleaved 19-fold faster than 3'ovr dsRNA in the absence of Loqs-PD, addition of this accessory factor decreases the rate difference to about 2-fold.

A model for cleavage by the *C. elegans* antiviral complex

As illustrated in Figure 6, a key feature of the antiviral complex is the interaction of DRH-1's NTD with DCR-1's helicase domain. When assaying DRH-1 alone, we observed ATP hydrolysis only when the NTD was removed (Figure 5), and we speculate this autoinhibition is relieved by interaction with DCR-1's helicase domain. While we only observe density for a single

dsRBM in each of our structures, in the models of Figure 6 we show all three motifs of RDE-4, consistent with other models of Dicer and dsRBPs[40,41]. By analogy to roles of dsRBMs in RNase III enzymes, it is possible that one or more of RDE-4's dsRBMs stabilizes dsRNA in a bent conformation that facilitates catalysis[34]. Hence, in our model, RDE-4 positions dsRNA in the RNase III active sites for ATP-independent and -dependent mechanisms (illustration 4 in Figure 6A); however, future studies will be required to validate this.

In the absence of nucleotide or in the presence of ATPγS, our cryo-EM structures show DRH-1 binding to the end of dsRNA, while addition of ATP shows DRH-1 localized to internal regions, consistent with the idea that DRH-1 translocates along dsRNA. We also observed that DRH-1 hydrolyzes ATP in a terminus-dependent manner (Figure 5), and thus, we show DRH-1 as the entry point for dsRNA (illustration 1 in Figure 6A), and by analogy to RLRs, propose that DRH-1 uses the energy of ATP hydrolysis to discriminate BLT and 3'ovr dsRNA, or nonself versus self[56]. As yet, how dsRNA proceeds from interacting exclusively with DRH-1 to then associating with DCR-1 for cleavage is unclear. As depicted, in our favorite model there is a conformational change that is more probable after recognition of a BLT terminus by DRH-1, that juxtaposes the dsRNA-bound helicase domain of DRH-1 with DCR-1's helicase domain for subsequent threading to the RNase III active site (illustrations 2 and 3 in Figure 6A). While our studies indicate DRH-1 plays the major role in ATP hydrolysis, our studies of a Walker A mutation in DCR-1 indicate its helicase domain also contributes to ATP hydrolysis and is required to produce an ATP-dependent 27mer when processing BLT dsRNA (Figure 2A). This suggests DCR-1 is involved in recognizing the BLT terminus, and thus we show dsRNA interacting with DCR-1’s helicase domain. We show dsRNA threading processively through the complex, as suggested by our trap experiments, as well as experiments showing that a mutation in DRH-1's helicase domain precludes generation of internal siRNAs (Figure 5). Since the K320A mutation in DRH-1's helicase domain precludes ATP hydrolysis (Figure 2F), the

cleavage observed from the ^{32}P-labeled dsRNA terminus either occurs without ATP hydrolysis (Figure 2A) or relies solely on hydrolysis from DCR-1. While the complex containing DRH-1^{K320A} does not show detectable hydrolysis, we cannot exclude the possibility that low levels of hydrolysis by DCR-1 are below the sensitivity of our assay. These observations suggest that production of the initial siRNA from a dsRNA end does not require DRH-1's ATP hydrolysis activity, but continued threading does.

In our 7.6Å structure acquired in the absence of ATP or with ATPγS, we observed one dsRNA interacting with DCR-1, and one with DRH-1, and speculate dsRNA associated with DCR-1 is poised for ATP-independent cleavage mediated by the Platform•PAZ domain (Figure 6B). We note however, that this structure would also be consistent with a mechanism whereby, after interaction with DRH-1, the dsRNA is handed off to DCR-1 without threading.

Why does *C. elegans* Dicer require accessory factors?

While it seems likely that Dicer was dedicated to antiviral defense in the common ancestor of animals[61,62], modern day animal Dicers have multiple roles, including processing dsRNA to produce mature miRNAs and endogenous siRNAs, and for invertebrates, processing viral dsRNA to produce viral siRNAs. In Arthropods, gene duplication led to Dicer enzymes specialized for different functions. *Drosophila melanogaster* uses dmDcr-1 for miRNA processing and dmDcr2 for processing viral dsRNA in the antiviral response. There is a need for specialization since recognition of a pre-miRNA, and the single round of distributive cleavage that generates a mature miRNA[37,63], places different demands on Dicer than the recognition of a nonself viral dsRNA and the processive cleavage that most efficiently processes viral dsRNA to siRNA.

H. sapiens and *C. elegans* have only a single Dicer, and it is interesting to compare how these organisms have delegated requisite functions. To deal with antiviral defense, vertebrates, including humans, use RLRs to recognize viral dsRNA and trigger an interferon response. Presumably this allowed human Dicer to specialize for miRNA processing. *C. elegans* does not have an interferon pathway, and its single Dicer enzyme is responsible for processing miRNAs, producing endogenous siRNAs, and promoting a robust antiviral response. An attractive idea is that accessory factors are key to allowing DCR-1 to function in these multiple pathways and to discriminate between different dsRNA substrates. Interestingly, *C. elegans* Dicer interacts with distinct RLR orthologs for its different functions. Our study focused on characterizing the antiviral complex, but another RLR homolog, DRH-3, associates with *C. elegans* DCR-1 to produce endogenous siRNA[26]. DRH-3 has been biochemically characterized and, like DRH-1, has robust ATP hydrolysis activity[64].

Materials and Methods

Plasmids and Cloning

DCR-1•DRH-1•RDE-4, DCR-1^{G36R}•DRH-1•RDE-4, DCR-1•DRH-1^{K320A}•RDE-4, and DCR-1•DRH-1 constructs were cloned into one vector as described (Weissmann *et al*., 2016). Briefly, for DCR-1•DRH-1•RDE-4, the coding sequences of *dcr-1*, *drh-1*, and *rde-4* were separately amplified using primers that contained overhangs to allow insertion of each gene between the BamHI and HIndIII sites of the plib vector to create a gene expression cassette (GEC) consisting of a polyhedrin promoter (polh), cDNA of gene, and SV40-terminator (term). The circularized products were transformed into DH5α chemically competent cells. Individual colonies were isolated, plasmids purified, and sent to Genewiz to confirm sequence of each GEC. The *dcr-1* GEC was amplified with cas III forward and cas V reverse primers, the *drh-1* GEC was amplified with cas I forward and cas I reverse primers, and the *rde-4* GEC was amplified with cas II forward and cas II reverse primers. The linearized pBig1b vector and PCR products were recombined in a Gibson assembly reaction using NEBuilder HiFi DNA Assembly Master Mix to create a circular product containing a polygene cassette (PGC). The circular product was transformed into MegaX DH10B T1 electrocompetent cells. Plasmids were purified from individual colonies and the SwaI and PmeI restriction sites were used to analyze the presence of all three genes. Plasmids that showed the correct digest patterns were sent to Genewiz to confirm the presence and sequence of each gene. Plib constructs were used as templates for site-directed mutagenesis to introduce point mutations in the Walker A sequences to create DCR-1^{G36R} and DRH-1^{K320A}. We then followed the necessary steps to insert the indicated coding sequences into the pBig1b vector to create the other PGCs: DCR-1^{G36R}•DRH-1•RDE-4, DCR-1•DRH-1^{K320A}•RDE-4, and DCR-1•DRH-1.

Expression System

Protein complexes were expressed in *Spodoptera frugiperda* (Sf9) cells using the modified Bac-to-Bac Baculovirus Expression System as described (Sinha and Bass, 2017).

Protein Purification

Protein complexes were purified using a modified method of (Sinha and Bass, 2017) to optimize for *C. elegans* proteins. Cell pellets were resuspended in 5.5 times the pellet volume in buffer (25mM HEPES [pH 7.5]; 10mM KOAc; 2mM $Mg(OAc)_2$; 100mM KCl; 1mM TCEP; 10% glycerol) supplemented with 1% Triton X-100, 20 nM Avidin, 250 mg/ml DNase I Grade II, cOmplete EDTA-free protease inhibitor (1 tablet per 25 ml buffer), 0.7% (vol/vol) Protease Inhibitor Cocktail, and 1 mM phenylmethanesulfonyl fluoride (PMSF). Cells were lysed by douncing on ice and lysates were clarified by ultracentrifugation and filtered through a 0.45uM low protein-binding filter. Filtered supernatant was bound to a 5 ml StrepTrap HP column pre-equilibrated in buffer. The column was washed with buffer (30ml), buffer supplemented with 5 mM ATP (30ml), and a final wash with buffer (30ml). Protein complexes were eluted in buffer supplemented with 2.5 mM d-Desthiobiotin. Pooled fractions were concentrated to ~500ul in a Vivaspin 20 protein concentrator and loaded onto a Superose 6 Increase 10/300 column pre-equilibrated with buffer. Pooled fractions were concentrated to ~0.5-1mg/ml in a Vivaspin 20 protein concentrator supplemented with 20% glycerol and flash frozen in liquid nitrogen.

dsRNA Preparation

106 nucleotide (nt) RNAs were prepared as described (Sinha *et al*., 2015 and Sinha *et al*., 2017). 52nt and 42 nt RNAs were chemically synthesized by University of Utah DNA/RNA Synthesis Core or IDT. Equimolar amounts of ssRNAs were annealed in annealing buffer (50 mM TRIS pH 8.0, 20 mM KCl) by placing the reaction on a heat block (95°C) and slow cooling ≥2 hr.

dsRNA Sequences

106 nt sense RNA: 5'-
GGCAAUGAAAGACGGUGAGCUGGUGAUAUGGGAUAGUGUUCACCCUUGUUACACCGUU
UUCCAUGAGCAAACUGAAACGUUUUCAUCGCUCUGGAGUGAAUACCAA-3'
106 nt antisense BLT RNA: 5'-
UUGGUAUUCACUCCAGAGCGAUGAAAACGUUUCAGUUUGCUCAUGGAAAACGGUGUAAC
AAGGGUGAACACUAUCCCAUAUCACCAGCUCACCGUCUUUCAUUGCC-3'
106 nt antisense 3'ovr RNA: 5'-
GGUAUUCACUCCAGAGCGAUGAAAACGUUUCAGUUUGCUCAUGGAAAACGGUGUAACAA
GGGUGAACACUAUCCCAUAUCACCAGCUCACCGUCUUUCAUUGCCAA-3'
52 nt sense RNA: 5'-
GGAGGUAGUAGGUUGUAUAGUAGUAAGACCAGACCCUAGACCAAUUCAUGCC-3'
52 nt antisense BLT RNA: 5'-
GGCAUGAAUUGGUCUAGGGUCUGGUCUUACUACUAUACAACCUACUACCUCC-3'
42 nt sense RNA: 5'-GGGAAGCUCAGAAUAUUGCACAAGUAGAGCUUCUCGAUCCCC-3'
42 nt antisense BLT RNA: 5'-
GGGGAUCGAGAAGCUCUACUUGUGCAAUAUUCUGAGCUUCCC-3'

Cleavage Assays

Reactions were at 20°C for times indicated in cleavage buffer (25mM HEPES [pH 7.5], 50mM KCl, 10mM $Mg(OAc)_2$, 1mM TCEP) with protein and dsRNA as specified, ± 5mM ATP-$MgOAc_2$ or ATPγS-$MgOAc_2$. Reactions were started by adding indicated protein complex and stopped with 2 volumes of 2X formamide loading buffer (95% formamide, 18mM EDTA, 0.025% SDS, xylene cyanol, bromophenol blue). Products were separated on an 8M Urea 17% denaturing PAGE gel, visualized on a PhosphorImager screen, and quantified with ImageQuant software. (Cleaved dsRNA / total dsRNA) x 100 = % dsRNA cleaved. Cleaved dsRNA is defined as all RNA products below the 106nt band. Total dsRNA is defined as the 106nt band plus all RNA products below the 106nt band. GraphPad Prism version 9 was used for curve-fitting analysis. Data were fit to the pseudo-first-order equation $y = y_o + A \times (1-e^{-kt})$; where y = product formed (% dsRNA cleaved); A = amplitude of the rate curve, y_o = baseline (~0), k = pseudo-first-order rate constant = k_{obs} ; t = time. Dotted line in graphs refers to the plateau constrained to 81.02 to compare the efficiency of all cleavage reactions to the wildtype complex with BLT dsRNA and ATP. For reactions with hexokinase and glucose, hexokinase (1 or 2 units as indicated) and glucose (10 mM) were incubated in reaction mix containing ± 5mM ATP (20 min; 20 C) to deplete ATP (or contaminating ATP) before adding DCR-1•DRH-1•RDE-4.

ATP Hydrolysis Assays

Reactions were at 20°C for times indicated in cleavage buffer with 25nM protein and 400nM dsRNA as specified, and 100uM ATP-$MgOAc_2$ plus 100nM [α-^{32}P] ATP-$MgOAc_2$ (3000 Ci/mmol)

to monitor hydrolysis. Reactions were started by adding protein, stopped at indicated times in equal volume of 0.5M EDTA, spotted onto PEI-cellulose plates, and chromatographed with 0.75M KH_2PO_4 (adjusted to pH 3.3 with H_3PO_4) until solvent reached top of plate. Plates were dried and visualized on a PhosphorImager screen. ADP and ATP radioactivity signals in TLC plates were quantified with ImageQuant software. (ADP / (ADP + ATP)) x 100 = % ADP product formed. GraphPad Prism version 9 was used for curve-fitting analysis. Data were fit to the pseudo-first-order equation as described in cleavage assays quantification. Dotted line in graphs refers to the plateau constrained to 89.55 to compare the efficiency of all cleavage reactions to the wildtype complex with BLT dsRNA.

Gel Mobility-Shift Assays

Gel mobility shift assays were performed with 20pM 106-basepair BLT or 3'ovr dsRNA, with sense strand labeled with ^{32}P at the 5' terminus and a 2', 3'-cyclic phosphate. Labeled dsRNA was incubated and allowed to reach equilibrium (45 min, 4°C) with wildtype DCR-1•DRH-1•RDE-4 complex, or indicated variant complex, in the presence and absence of 5mM ATP-$MgOAc_2$, in binding buffer (25 mM HEPES pH 8.0, 100 mM KCl, 10 mM $MgCl_2$, 10% (vol/vol) glycerol, 1 mM TCEP); final reaction volume, 20 *µ*l. Protein complex was serially diluted in binding buffer before addition to binding reaction. Reactions were stopped by loading directly onto a 4% polyacrylamide (29:1 acrylamide/bisacrylamide) native gel running at 200V at 4°C, in 0.5X Tris/Borate/EDTA running buffer. The gel was pre-run (30 min) before loading samples. Gels were electrophoresed (3 hr) to resolve complex-bound dsRNA from free dsRNA, dried (80°C, 1 hr) and exposed overnight to a Molecular Dynamics Storage Phosphor Screen. Radioactivity signal was visualized on a Typhoon PhosphorImager (GE Healthcare LifeSciences) in the linear dynamic range of the instrument and quantified using ImageQuant version 8 software. Radioactivity in gels corresponding to $dsRNA_{total}$ and $dsRNA_{free}$ was quantified to determine fraction bound. Fraction bound = 1 – ($dsRNA_{free}$ / $dsRNA_{total}$). All dsRNA that migrated through the gel more slowly than $dsRNA_{free}$ was considered as bound to the complex. To determine K_d values, binding isotherms were fit using the Hill formalism, where fraction bound = $1 / (1 + (K_d^n/[P]^n))$; K_d = equilibrium dissociation constant, n = Hill coefficient, [P] = protein concentration. GraphPad Prism version 9 was used for curve-fitting analysis.

Trap Assays

Reactions were at 20°C for times indicated in cleavage buffer (25mM HEPES [pH 7.5], 50mM KCl, 10mM $Mg(OAc)_2$, 1mM TCEP) with 50nM protein and 1nM ^{32}P internally labeled 106 BLT dsRNA with 5mM ATP ± 2000nM 52 BLT cold dsRNA. Reactions were started by adding dsRNA and stopped with 2 volumes of 2X formamide loading buffer (95% formamide, 18mM EDTA, 0.025% SDS, xylene cyanol, bromophenol blue). Products were separated on an 8M Urea 17% denaturing PAGE gel, visualized on a PhosphorImager screen, and quantified with ImageQuant software. (siRNA/total counts) x 100 = % siRNA product formed. GraphPad Prism version 9 was used for curve-fitting analysis. Data were fit to the pseudo-first-order equation as described in cleavage assays quantification.

Cryo-EM specimen preparation

UltrAuFoil R2/2 Au300 mesh grids (Quantifoil) were glow discharged for 30 seconds on each side at 25 mA using a Pelco easiGlow unit (Ted Pella, Inc.). 3.5 µl of purified complex (0.8-1 µM concentration) with 1.5x molar excess dsRNA with or without 5mM nucleotide (ATP or ATPγS)

and 5% glycerol was applied to the grid and blotted with filter paper (595 Filter Paper, Ted Pella, Inc.) for 5 seconds using an Mk. II Vitrobot (Thermo Fisher Scientific) with a −1 mm offset and then plunge frozen into liquid ethane. For the sample that led to the DRH-1 bound to dsRNA reconstruction, the complex was purified as described above, except with 2mM CaCl2 instead of 2mM $Mg(OAc)^2$. 2mM $Mg(OAc)^2$ was added to the sample before it was applied to the grid.

Cryo-EM and data processing of complex bound to two dsRNAs

For the complex bound to two dsRNAs, cryo-EM movies were recorded using SerialEM v3.840[73] at the Pacific Northwest CryoEM Center. Images were recorded in super-resolution mode on a 300 kV Titan Krios (Thermo Fisher Scientific) equipped with a post-GIF K3 direct detector (Gatan, Inc.), using a nominal magnification of 81,000x, corresponding to a super-resolution pixel size of 0.394Å, with a total dose of 50 electrons/$Å^2$ and 50 frames per movie. Super-resolution cryo-EM movie frames were motion corrected, dose-weighted, Fourier binned 2x, and summed using CryoSPARC v3.3.233[74]. CTF parameters were determined using patch CTF estimation. A total of 3,866 micrographs displayed CTF resolution fits of 6 Å or better and were used for downstream analysis. Particles were blob picked with a range of 225-375Å diameter to obtain initial 2D classes for template-based picking. Particles were extracted at a box size of 300. During earlier processing steps, the box was 4x binned but was extracted at the original box size of 300 for final reconstructions. After multiple rounds of template-based picking, a total of 324,464 particles were obtained, through which 70,904 of the best particles were selected and run through ab initio reconstruction. The best volume comprised 26,879 particles and revealed two dsRNA molecules interacting with the complex. A final homogeneous refinement job yielded a 7.6 Å reconstruction map that was used for rigid-body fitting of individual components.

Cryo-EM and data processing of complex bound to one dsRNA

For the dataset yielding the reconstruction of the complex bound to one dsRNA, cryo-EM movies were recorded at a nominal magnification of 81,000×, corresponding to a super resolution pixel size of 0.533Å, with a total dose of 50 electrons/$Å^2$ and 40 frames per movie. Data were collected using Leginon[75] at the National Center for CryoEM Access and Training (New York Structural Biology Center). Super-resolution cryo-EM movie frames were motion corrected, dose-weighted, Fourier binned 2x, and summed using CryoSPARC v3.3.233[74]. Two separate datasets were collected of this complex, one with and one without added ATPγS. Separate processing of each dataset did not reveal noticeable differences, thus rationalizing the combining of the particles into one project. A total of 24,705 micrographs displaying CTF resolution fits of 6 Å or better were used for downstream analysis. Particles were selected from a combination of blob and template-based picking, then extracted at a box size of 384 pixels and 4x binned for initial 2D classification. After several rounds of template-based picking from original blob-based picks (225-300Å), 317,291 particles were used for 2D classification, and 314,554 particles were used for ab initio reconstruction. Unbinned particles (384 pixel box size) were used for final reconstructions. The volume with the best density for the entire complex with dsRNA bound (171,304 particles) were used for homogeneous and local refinement, yielding a final reconstruction at 6.1 Å resolution.

Cryo-EM and data processing of DRH-1 bound to dsRNA

For the reconstruction of the DRH-1 dataset with calcium, magnesium, the complex, and 3'ovr 106 dsRNA, cryo-EM movies were recorded at a nominal magnification of 81,000x,

corresponding to a super-resolution pixel size of 0.529Å with a total dose of 38 electrons/Å^2 and 40 frames per movie.
Movies were patch motion corrected and CTF estimated in CryoSPARC v3.3.233[74], and a total of 14,602 micrographs displaying CTF resolution fits of 6 Å or better were used for downstream analysis. Particles were selected using blob-based picking (225-300 Å diameter). After several rounds of 2D classification, a total of 759,994 were used for ab initio reconstruction (4 classes). After removing junk classes, a total of 591,250 particles were used for heterogeneous refinement (4 classes). This led to 2 similar, well-resolved classes comprising 362,869 particles that were then used for high-resolution 3D reconstruction. The particles were first subject to non-uniform refinement, producing a 3.1 Å map. Finally, local refinement of the same particles was performed using a mask that focused on DRH-1 density. This produced a final 2.9 Å map that was used for model building and refinement.
Data processing workflows for all three reconstructions are available in Figures S7F, S8F, and Table S2.

Interpretation of DCR-1::DRH-1::RDE4::dsRNA reconstructions
For the densities for DCR-1 and RDE-4, we used the human model for rigid body fitting (PDB 5ZAK)[40]. We also used the human model for rigid body fitting of DCR-1::RDE::dsRNA (PDB 5ZAL)[40]. In both reconstructions of the complex, we used the AlphaFold2[44,45] model to fit DRH-1 (AF-G5EDI8-F1). The NTD and helicase domains of DRH-1 were fit separately to accommodate the different orientation of the NTD in the AlphaFold2 model compared to the density. We generated an A-form dsRNA in UCSF Chimera[69] to fit into the density of the dsRNA interacting with DRH-1's helicase.

Model Building, Refinement, and Validation of DRH-1:dsRNA structure
The model for DRH-1 was built manually in the 2.9 Å density map using Coot v0.8.9.1[76]. The AlphaFold2[44,45] model as a starting point (AF-G5EDI8-F1). The ADP ligand was built using Phenix[77] Ligand Fit tool, while the Mg^{2+} and Zn^{2+} substrates were manually built in Coot. We used a 106nt dsRNA in the sample; however, the density of dsRNA in the final reconstruction was shorter than 106 bp and likely represents a mixture of positions bound by DRH-1. We therefore generated a 30-nucleotide A:U base paired dsRNA in Coot to use for modeling. The model and substrates were subjected to real-space refinement using Phenix v1.20.1-4487. Default settings were used, except the weight was set to 0.01.

Analytical ultracentrifugation
Sedimentation velocity analytical ultracentrifugation (Beckman Coulter Optima XL-I) of DCR-1•DRH-1•RDE-4 and DCR-1•DRH-1 after purification by size exclusion chromatography in 25 mM HEPES pH 7.5, 10 mM KOAc, 2 mM $Mg(OAc)_2$, 100 mM KCl, 1mM TCEP. Samples (420 µL) at 0.4 A 280nm (for DCR-1•DRH-1•RDE-4) and 0.3 A 280nm (for DCR-1•DRH-1) and matching buffer (440 µL) were centrifuged at 40,000 RPM in carbon epon 2-sector centerpieces loaded in an An60-Ti rotor. Radial distributions were recorded continuously via absorbance at 280 nm (0.003 radial step size, 1 replicate) and 20 ºC. Buffer density (ρ) (1.005 g/mL), monomeric molecular weights (386,825 Da for DCR-1•DRH-1•RDE-4 and 343,417 Da for DCR-1•DRH-1), and partial specific volumes (0.7348 mL/g for DCR-1•DRH-1•RDE-4 and 0.735 mL/g for DCR-1•DRH-1) were calculated with SEDNTERP[78]. The c(s) continuous sedimentation distribution function of the data was determined via analysis by SEDFIT using alternating

Marquardt-Levenberg and simplex algorithms, with an F-ratio of 0.68, representing one standard deviation[79]. The c(s) analysis and data/fit/residuals were exported from SEDFIT and plotted with the GUSSI software[80].

Acknowledgments

We thank the Bass and Shen labs for helpful feedback, M. Salemi at UC Davis Proteomics Core for assistance with mass spectrometry, S. Wang for assistance with structural biology methodology, and T. Duchaine for providing RDE-4 antibodies. DNA synthesis and flow cytometry (Office of The Director of the NIH, S10OD026959) was performed at the University of Utah Core Facilities. For the cryo-EM work, we acknowledge D. Belanp at the University of Utah Electron Microscopy Core Laboratory, O. Davulcu PNCC at OHSU (NIH grant U24GM129547), and H. Kuang at NYSBC (NIH Common Fund Transformative High Resolution Cryo-Electron Microscopy program U24 GM129539, and by grants from the Simons Foundation, SF349247, and NY State Assembly). PNCC data was accessed through EMSL (grid.436923.9), a DOE Office of Science User Facility sponsored by the Office of Biological and Environmental Research and data for PNCC was accessed through EMSL, and data for NYSBC was accessed through Globus. We also thank I. Allen and A. Orendt at the Utah Center for High-Performance Computing for computational support. C.D.C was supported by the National Institutes of Health under Ruth L. Kirschstein National Research Service Award NIH T32AI055434 from the National Institute of Allergy and Infectious Diseases (NIAID). This work was supported by funding to B.L.B from the National Institute of General Medical Sciences (R35GM141262) and the National Cancer Institute of the National Institutes of Health (R01CA260414) and to P.S.S. from the National Institute of General Medical Sciences (R35GM133772).

References

1. Dumesic, P.A., and Madhani, H.D. (2014). Recognizing the enemy within: licensing RNA-guided genome defense. Trends Biochem Sci *39*, 25–34. 10.1016/j.tibs.2013.10.003.

2. Koonin, E.V. (2017). Evolution of RNA- and DNA-guided antivirus defense systems in prokaryotes and eukaryotes: common ancestry vs convergence. Biol Direct *12*, 5. 10.1186/s13062-017-0177-2.

3. Gutbrod, M.J., and Martienssen, R.A. (2020). Conserved chromosomal functions of RNA interference. Nat Rev Genet *21*, 311–331. 10.1038/s41576-019-0203-6.

4. Cullen, B.R., Cherry, S., and tenOever, B.R. (2013). Is RNA Interference a Physiologically Relevant Innate Antiviral Immune Response in Mammals? Cell Host Microbe *14*, 374–378. 10.1016/j.chom.2013.09.011.

5. Poirier, E.Z., Buck, M.D., Chakravarty, P., Carvalho, J., Frederico, B., Cardoso, A., Healy, L., Ulferts, R., Beale, R., and Sousa, C.R. e (2021). An isoform of Dicer protects mammalian stem cells against multiple RNA viruses. Science *373*, 231–236. 10.1126/science.abg2264.

6. Wilson, R.C., and Doudna, J.A. (2013). Molecular Mechanisms of RNA Interference. Annu Rev Biophys *42*, 217–239. 10.1146/annurev-biophys-083012-130404.

7. Ciechanowska, K., Pokornowska, M., and Kurzyńska-Kokorniak, A. (2021). Genetic Insight into the Domain Structure and Functions of Dicer-Type Ribonucleases. Int J Mol Sci *22*, 616. 10.3390/ijms22020616.

8. Jiang, F., Ye, X., Liu, X., Fincher, L., McKearin, D., and Liu, Q. (2005). Dicer-1 and R3D1-L catalyze microRNA maturation in Drosophila. Gene Dev *19*, 1674–1679. 10.1101/gad.1334005.

9. Tsutsumi, A., Kawamata, T., Izumi, N., Seitz, H., and Tomari, Y. (2011). Recognition of the pre-miRNA structure by Drosophila Dicer-1. Nat Struct Mol Biol *18*, 1153–1158. 10.1038/nsmb.2125.

10. Welker, N.C., Maity, T.S., Ye, X., Aruscavage, P.J., Krauchuk, A.A., Liu, Q., and Bass, B.L. (2011). Dicer's Helicase Domain Discriminates dsRNA Termini to Promote an Altered Reaction Mode. Mol Cell *41*, 589–599. 10.1016/j.molcel.2011.02.005.

11. Sinha, N.K., Iwasa, J., Shen, P.S., and Bass, B.L. (2018). Dicer uses distinct modules for recognizing dsRNA termini. Science *359*, 329–334. 10.1126/science.aaq0921.

12. Marques, J.T., Wang, J.-P., Wang, X., Oliveira, K.P.V. de, Gao, C., Aguiar, E.R.G.R., Jafari, N., and Carthew, R.W. (2013). Functional Specialization of the Small Interfering RNA Pathway in Response to Virus Infection. PLoS Pathogens *9*, e1003579. 10.1371/journal.ppat.1003579.

13. Donelick, H.M., Talide, L., Bellet, M., Aruscavage, P.J., Lauret, E., Aguiar, E.R.G.R., Marques, J.T., Meignin, C., and Bass, B.L. (2020). In vitro studies provide insight into effects of Dicer-2 helicase mutations in Drosophila melanogaster. RNA *26*, 1847–1861. 10.1261/rna.077289.120.

14. Sinha, N.K., Trettin, K.D., Aruscavage, P.J., and Bass, B.L. (2015). Drosophila Dicer-2 Cleavage Is Mediated by Helicase- and dsRNA Termini-Dependent States that Are Modulated by Loquacious-PD. Mol Cell *58*, 406–417. 10.1016/j.molcel.2015.03.012.

15. Singh, R.K., Jonely, M., Leslie, E., Rejali, N.A., Noriega, R., and Bass, B.L. (2021). Transient kinetic studies of the antiviral Drosophila Dicer-2 reveal roles of ATP in self–nonself discrimination. Elife *10*, e65810. 10.7554/elife.65810.

16. Ma, E., MacRae, I.J., Kirsch, J.F., and Doudna, J.A. (2008). Autoinhibition of Human Dicer by Its Internal Helicase Domain. J Mol Biol *380*, 237–243. 10.1016/j.jmb.2008.05.005.

17. Ahmad, S., and Hur, S. (2015). Helicases in Antiviral Immunity: Dual Properties as Sensors and Effectors. Trends Biochem Sci *40*, 576–585. 10.1016/j.tibs.2015.08.001.

18. Luo, D., Kohlway, A., and Pyle, A.M. (2013). Duplex RNA activated ATPases (DRAs). RNA Biology *10*, 111–120. 10.4161/rna.22706.

19. Kowalinski, E., Lunardi, T., McCarthy, A.A., Louber, J., Brunel, J., Grigorov, B., Gerlier, D., and Cusack, S. (2011). Structural Basis for the Activation of Innate Immune Pattern-Recognition Receptor RIG-I by Viral RNA. Cell *147*, 423–435. 10.1016/j.cell.2011.09.039.

20. Luo, D., Ding, S.C., Vela, A., Kohlway, A., Lindenbach, B.D., and Pyle, A.M. (2011). Structural Insights into RNA Recognition by RIG-I. Cell *147*, 409–422. 10.1016/j.cell.2011.09.023.

21. Rehwinkel, J., and Gack, M.U. (2020). RIG-I-like receptors: their regulation and roles in RNA sensing. Nat Rev Immunol, 1–15. 10.1038/s41577-020-0288-3.

22. Schlee, M., Roth, A., Hornung, V., Hagmann, C.A., Wimmenauer, V., Barchet, W., Coch, C., Janke, M., Mihailovic, A., Wardle, G., et al. (2009). Recognition of 5′ Triphosphate by RIG-I Helicase Requires Short Blunt Double-Stranded RNA as Contained in Panhandle of Negative-Strand Virus. Immunity *31*, 25–34. 10.1016/j.immuni.2009.05.008.

23. Peisley, A., Lin, C., Wu, B., Orme-Johnson, M., Liu, M., Walz, T., and Hur, S. (2011). Cooperative assembly and dynamic disassembly of MDA5 filaments for viral dsRNA recognition. Proc National Acad Sci *108*, 21010–21015. 10.1073/pnas.1113651108.

24. Veen, A.G., Maillard, P.V., Schmidt, J.M., Lee, S.A., Deddouche-Grass, S., Borg, A., Kjær, S., Snijders, A.P., and Sousa, C.R. e (2018). The RIG-I-like receptor LGP2 inhibits Dicer-dependent processing of long double-stranded RNA and blocks RNA interference in mammalian cells. EMBO *37*. 10.15252/embj.201797479.

25. Montavon, T.C., Baldaccini, M., Lefèvre, M., Girardi, E., Chane-Woon-Ming, B., Messmer, M., Hammann, P., Chicher, J., and Pfeffer, S. (2021). Human DICER helicase domain recruits PKR and modulates its antiviral activity. PLoS Pathogens *17*, e1009549. 10.1371/journal.ppat.1009549.

26. Thivierge, C., Makil, N., Flamand, M., Vasale, J.J., Mello, C.C., Wohlschlegel, J., Conte, D., and Duchaine, T.F. (2012). Tudor domain ERI-5 tethers an RNA-dependent RNA polymerase to DCR-1 to potentiate endo-RNAi. Nat Struct Mol Biol *19*, 90–97. 10.1038/nsmb.2186.

27. Ashe, A., Bélicard, T., Pen, J.L., Sarkies, P., Frézal, L., Lehrbach, N.J., Félix, M.-A., and Miska, E.A. (2013). A deletion polymorphism in the Caenorhabditis elegans RIG-I homolog disables viral RNA dicing and antiviral immunity. Elife *2*, e00994. 10.7554/elife.00994.

28. Guo, X., Zhang, R., Wang, J., Ding, S.-W., and Lu, R. (2013). Homologous RIG-I–like helicase proteins direct RNAi-mediated antiviral immunity in C. elegans by distinct mechanisms. Proc National Acad Sci *110*, 16085–16090. 10.1073/pnas.1307453110.

29. Tabara, H., Yigit, E., Siomi, H., and Mello, C.C. (2002). The dsRNA Binding Protein RDE-4 Interacts with RDE-1, DCR-1, and a DExH-Box Helicase to Direct RNAi in C. elegans. Cell *109*, 861–871. 10.1016/s0092-8674(02)00793-6.

30. Parker, G.S., Eckert, D.M., and Bass, B.L. (2006). RDE-4 preferentially binds long dsRNA and its dimerization is necessary for cleavage of dsRNA to siRNA. RNA *12*, 807–818. 10.1261/rna.2338706.

31. Parker, G.S., Maity, T.S., and Bass, B.L. (2008). dsRNA Binding Properties of RDE-4 and TRBP Reflect Their Distinct Roles in RNAi. J Mol Biol *384*, 967–979. 10.1016/j.jmb.2008.10.002.

32. Fire, A., Xu, S., Montgomery, M.K., Kostas, S.A., Driver, S.E., and Mello, C.C. (1998). Potent and specific genetic interference by double-stranded RNA in Caenorhabditis elegans. Nature *391*, 806–811. 10.1038/35888.

33. Cenik, E.S., Fukunaga, R., Lu, G., Dutcher, R., Wang, Y., Hall, T.M.T., and Zamore, P.D. (2011). Phosphate and R2D2 Restrict the Substrate Specificity of Dicer-2, an ATP-Driven Ribonuclease. Mol Cell *42*, 172–184. 10.1016/j.molcel.2011.03.002.

34. Hansen, S.R., Aderounmu, A.M., Donelick, H.M., and Bass, B.L. (2020). Dicer's Helicase Domain: A Meeting Place for Regulatory Proteins. Cold Spring Harb Sym, 039750. 10.1101/sqb.2019.84.039750.

35. Weissmann, F., Petzold, G., VanderLinden, R., Veld, P.J.H. in 't, Brown, N.G., Lampert, F., Westermann, S., Stark, H., Schulman, B.A., and Peters, J.-M. (2016). biGBac enables rapid gene assembly for the expression of large multisubunit protein complexes. Proc National Acad Sci *113*, E2564–E2569. 10.1073/pnas.1604935113.

36. Ruby, J.G., Jan, C., Player, C., Axtell, M.J., Lee, W., Nusbaum, C., Ge, H., and Bartel, D.P. (2006). Large-Scale Sequencing Reveals 21U-RNAs and Additional MicroRNAs and Endogenous siRNAs in C. elegans. Cell *127*, 1193–1207. 10.1016/j.cell.2006.10.040.

37. Park, J.-E., Heo, I., Tian, Y., Simanshu, D.K., Chang, H., Jee, D., Patel, D.J., and Kim, V.N. (2011). Dicer recognizes the 5′ end of RNA for efficient and accurate processing. Nature *475*, 201–205. 10.1038/nature10198.

38. Tian, Y., Simanshu, D.K., Ma, J.-B., Park, J.-E., Heo, I., Kim, V.N., and Patel, D.J. (2014). A Phosphate-Binding Pocket within the Platform-PAZ-Connector Helix Cassette of Human Dicer. Mol Cell *53*, 606–616. 10.1016/j.molcel.2014.01.003.

39. Singh, R.K., Jonely, M., Leslie, E., Rejali, N.A., Noriega, R., and Bass, B.L. (2021). Transient kinetic studies of the antiviral Drosophila Dicer-2 reveal roles of ATP in self–nonself discrimination. Elife *10*, e65810. 10.7554/elife.65810.

40. Liu, Z., Wang, J., Cheng, H., Ke, X., Sun, L., Zhang, Q.C., and Wang, H.-W. (2018). Cryo-EM Structure of Human Dicer and Its Complexes with a Pre-miRNA Substrate. Cell *173*, 1191-1203.e12. 10.1016/j.cell.2018.03.080.

41. Yamaguchi, S., Naganuma, M., Nishizawa, T., Kusakizako, T., Tomari, Y., Nishimasu, H., and Nureki, O. (2022). Structure of the Dicer-2–R2D2 heterodimer bound to a small RNA duplex. Nature *607*, 393–398. 10.1038/s41586-022-04790-2.

42. Lau, P.-W., Potter, C.S., Carragher, B., and MacRae, I.J. (2009). Structure of the Human Dicer-TRBP Complex by Electron Microscopy. Structure *17*, 1326–1332. 10.1016/j.str.2009.08.013.

43. Lau, P.-W., Guiley, K.Z., De, N., Potter, C.S., Carragher, B., and MacRae, I.J. (2012). The molecular architecture of human Dicer. Nat Struct Mol Biol *19*, 436–440. 10.1038/nsmb.2268.

44. Varadi, M., Anyango, S., Deshpande, M., Nair, S., Natassia, C., Yordanova, G., Yuan, D., Stroe, O., Wood, G., Laydon, A., et al. (2021). AlphaFold Protein Structure Database: massively expanding the structural coverage of protein-sequence space with high-accuracy models. Nucleic Acids Res *50*, D439–D444. 10.1093/nar/gkab1061.

45. Jumper, J., Evans, R., Pritzel, A., Green, T., Figurnov, M., Ronneberger, O., Tunyasuvunakool, K., Bates, R., Žídek, A., Potapenko, A., et al. (2021). Highly accurate protein structure prediction with AlphaFold. Nature *596*, 583–589. 10.1038/s41586-021-03819-2.

46. Zhang, H., Kolb, F.A., Brondani, V., Billy, E., and Filipowicz, W. (2002). Human Dicer preferentially cleaves dsRNAs at their termini without a requirement for ATP. EMBO *21*, 5875–5885. 10.1093/emboj/cdf582.

47. Zhang, H., Kolb, F.A., Jaskiewicz, L., Westhof, E., and Filipowicz, W. (2004). Single Processing Center Models for Human Dicer and Bacterial RNase III. Cell *118*, 57–68. 10.1016/j.cell.2004.06.017.

48. Cordin, O., Tanner, N.K., Doère, M., Linder, P., and Banroques, J. (2004). The newly discovered Q motif of DEAD-box RNA helicases regulates RNA-binding and helicase activity. EMBO J. *23*, 2478–2487. 10.1038/sj.emboj.7600272.

49. Fairman-Williams, M.E., Guenther, U.-P., and Jankowsky, E. (2010). SF1 and SF2 helicases: family matters. Curr. Opin. Struct. Biol. *20*, 313–324. 10.1016/j.sbi.2010.03.011.

50. Civril, F., Bennett, M., Moldt, M., Deimling, T., Witte, G., Schiesser, S., Carell, T., and Hopfner, K. (2011). The RIG-I ATPase domain structure reveals insights into ATP-dependent antiviral signalling. EMBO Rep. *12*, 1127–1134. 10.1038/embor.2011.190.

51. Wu, B., Peisley, A., Richards, C., Yao, H., Zeng, X., Lin, C., Chu, F., Walz, T., and Hur, S. (2013). Structural Basis for dsRNA Recognition, Filament Formation, and Antiviral Signal Activation by MDA5. Cell *152*, 276–289. 10.1016/j.cell.2012.11.048.

52. Yu, Q., Qu, K., and Modis, Y. (2018). Cryo-EM Structures of MDA5-dsRNA Filaments at Different Stages of ATP Hydrolysis. Mol Cell *72*, 999-1012.e6. 10.1016/j.molcel.2018.10.012.

53. Devarkar, S.C., Wang, C., Miller, M.T., Ramanathan, A., Jiang, F., Khan, A.G., Patel, S.S., and Marcotrigiano, J. (2016). Structural basis for m7G recognition and 2′-O-methyl discrimination in capped RNAs by the innate immune receptor RIG-I. Proc. Natl. Acad. Sci. *113*, 596–601. 10.1073/pnas.1515152113.

54. Wang, W., and Pyle, A.M. (2022). The RIG-I receptor adopts two different conformations for distinguishing host from viral RNA ligands. Mol Cell *82*, 4131-4144.e6. 10.1016/j.molcel.2022.09.029.

55. Willemsen, J., Wicht, O., Wolanski, J.C., Baur, N., Bastian, S., Haas, D.A., Matula, P., Knapp, B., Meyniel-Schicklin, L., Wang, C., et al. (2017). Phosphorylation-Dependent Feedback Inhibition of RIG-I by DAPK1 Identified by Kinome-wide siRNA Screening. Mol. Cell *65*, 403-415.e8. 10.1016/j.molcel.2016.12.021.

56. Devarkar, S.C., Schweibenz, B., Wang, C., Marcotrigiano, J., and Patel, S.S. (2018). RIG-I Uses an ATPase-Powered Translocation-Throttling Mechanism for Kinetic Proofreading of RNAs and Oligomerization. Mol Cell *72*, 355-368.e4. 10.1016/j.molcel.2018.08.021.

57. Ramanathan, A., Devarkar, S.C., Jiang, F., Miller, M.T., Khan, A.G., Marcotrigiano, J., and Patel, S.S. (2016). The autoinhibitory CARD2-Hel2i Interface of RIG-I governs RNA selection. Nucleic Acids Res *44*, 896–909. 10.1093/nar/gkv1299.

58. Peisley, A., Wu, B., Yao, H., Walz, T., and Hur, S. (2013). RIG-I Forms Signaling-Competent Filaments in an ATP-Dependent, Ubiquitin-Independent Manner. Mol Cell *51*, 573–583. 10.1016/j.molcel.2013.07.024.

59. Coffman, S.R., Lu, J., Guo, X., Zhong, J., Jiang, H., Broitman-Maduro, G., Li, W.-X., Lu, R., Maduro, M., and Ding, S. (2017). Caenorhabditis elegans RIG-I Homolog Mediates Antiviral RNA Interference Downstream of Dicer-Dependent Biogenesis of Viral Small Interfering RNAs. mBio *8*, e00264-17. 10.1128/mbio.00264-17.

60. Lu, R., Yigit, E., Li, W.-X., and Ding, S.-W. (2009). An RIG-I-Like RNA Helicase Mediates Antiviral RNAi Downstream of Viral siRNA Biogenesis in Caenorhabditis elegans. PLoS Pathogens *5*, e1000286. 10.1371/journal.ppat.1000286.

61. Mukherjee, K., Campos, H., and Kolaczkowski, B. (2013). Evolution of Animal and Plant Dicers: Early Parallel Duplications and Recurrent Adaptation of Antiviral RNA Binding in Plants. Mol Biol Evol *30*, 627–641. 10.1093/molbev/mss263.

62. Aderounmu, A.M., Aruscavage, P.J., Kolaczkowski, B., and Bass, B.L. (2023). Ancestral protein reconstruction reveals evolutionary events governing variation in Dicer helicase function. eLife *12*, e85120. 10.7554/elife.85120.

63. Lee, Y.-Y., Lee, H., Kim, H., Kim, V.N., and Roh, S.-H. (2023). Structure of the human DICER–pre-miRNA complex in a dicing state. Nature, 1–8. 10.1038/s41586-023-05723-3.

64. Matranga, C., and Pyle, A.M. (2010). Double-stranded RNA-dependent ATPase DRH-3. J Biol Chem *285*, 25363–25371. 10.1074/jbc.m110.117010.

65. Marchler-Bauer, A., Lu, S., Anderson, J.B., Chitsaz, F., Derbyshire, M.K., DeWeese-Scott, C., Fong, J.H., Geer, L.Y., Geer, R.C., Gonzales, N.R., et al. (2011). CDD: a Conserved Domain Database for the functional annotation of proteins. Nucleic Acids Res *39*, D225–D229. 10.1093/nar/gkq1189.

66. Goujon, M., McWilliam, H., Li, W., Valentin, F., Squizzato, S., Paern, J., and Lopez, R. (2010). A new bioinformatics analysis tools framework at EMBL–EBI. Nucleic Acids Res *38*, W695–W699. 10.1093/nar/gkq313.

67. Sievers, F., Wilm, A., Dineen, D., Gibson, T.J., Karplus, K., Li, W., Lopez, R., McWilliam, H., Remmert, M., Söding, J., et al. (2011). Fast, scalable generation of high-quality protein multiple sequence alignments using Clustal Omega. Mol Syst Biol *7*, 539–539. 10.1038/msb.2011.75.

68. McWilliam, H., Li, W., Uludag, M., Squizzato, S., Park, Y.M., Buso, N., Cowley, A.P., and Lopez, R. (2013). Analysis Tool Web Services from the EMBL-EBI. Nucleic Acids Res *41*, W597–W600. 10.1093/nar/gkt376.

69. Pettersen, E.F., Goddard, T.D., Huang, C.C., Couch, G.S., Greenblatt, D.M., Meng, E.C., and Ferrin, T.E. (2004). UCSF Chimera—A visualization system for exploratory research and analysis. J. Comput. Chem. *25*, 1605–1612. 10.1002/jcc.20084.

70. Robert, X., and Gouet, P. (2014). Deciphering key features in protein structures with the new ENDscript server. Nucleic Acids Res. *42*, W320–W324. 10.1093/nar/gku316.

71. Lavery, R., Moakher, M., Maddocks, J.H., Petkeviciute, D., and Zakrzewska, K. (2009). Conformational analysis of nucleic acids revisited: Curves+. Nucleic Acids Res. *37*, 5917–5929. 10.1093/nar/gkp608.

72. Blanchet, C., Pasi, M., Zakrzewska, K., and Lavery, R. (2011). CURVES+ web server for analyzing and visualizing the helical, backbone and groove parameters of nucleic acid structures. Nucleic Acids Res. *39*, W68–W73. 10.1093/nar/gkr316.

73. Mastronarde, D.N. (2005). Automated electron microscope tomography using robust prediction of specimen movements. J. Struct. Biol. *152*, 36–51. 10.1016/j.jsb.2005.07.007.

74. Punjani, A., Rubinstein, J.L., Fleet, D.J., and Brubaker, M.A. (2017). cryoSPARC: algorithms for rapid unsupervised cryo-EM structure determination. Nat Methods *14*, 290–296. 10.1038/nmeth.4169.

75. Suloway, C., Pulokas, J., Fellmann, D., Cheng, A., Guerra, F., Quispe, J., Stagg, S., Potter, C.S., and Carragher, B. (2005). Automated molecular microscopy: The new Leginon system. J. Struct. Biol. *151*, 41–60. 10.1016/j.jsb.2005.03.010.

76. Emsley, P., Lohkamp, B., Scott, W.G., and Cowtan, K. (2010). Features and development of Coot. Acta Crystallogr. Sect. D: Biol. Crystallogr. *66*, 486–501. 10.1107/s0907444910007493.

77. Adams, P.D., Afonine, P.V., Bunkóczi, G., Chen, V.B., Davis, I.W., Echols, N., Headd, J.J., Hung, L.-W., Kapral, G.J., Grosse-Kunstleve, R.W., et al. (2010). PHENIX: a comprehensive Python-based system for macromolecular structure solution. Acta Crystallogr. Sect. D: Biol. Crystallogr. *66*, 213–221. 10.1107/s0907444909052925.

78. Philo, J.S. (2023). SEDNTERP: a calculation and database utility to aid interpretation of analytical ultracentrifugation and light scattering data. Eur. Biophys. J., 1–34. 10.1007/s00249-023-01629-0.

79. Schuck, P. (2000). Size-Distribution Analysis of Macromolecules by Sedimentation Velocity Ultracentrifugation and Lamm Equation Modeling. Biophys. J. *78*, 1606–1619. 10.1016/s0006-3495(00)76713-0.

80. Brautigam, C.A. (2015). Calculations and Publication-Quality Illustrations for Analytical Ultracentrifugation Data. Methods Enzym. *562*, 109–133. 10.1016/bs.mie.2015.05.001.

Main Figures and Tables

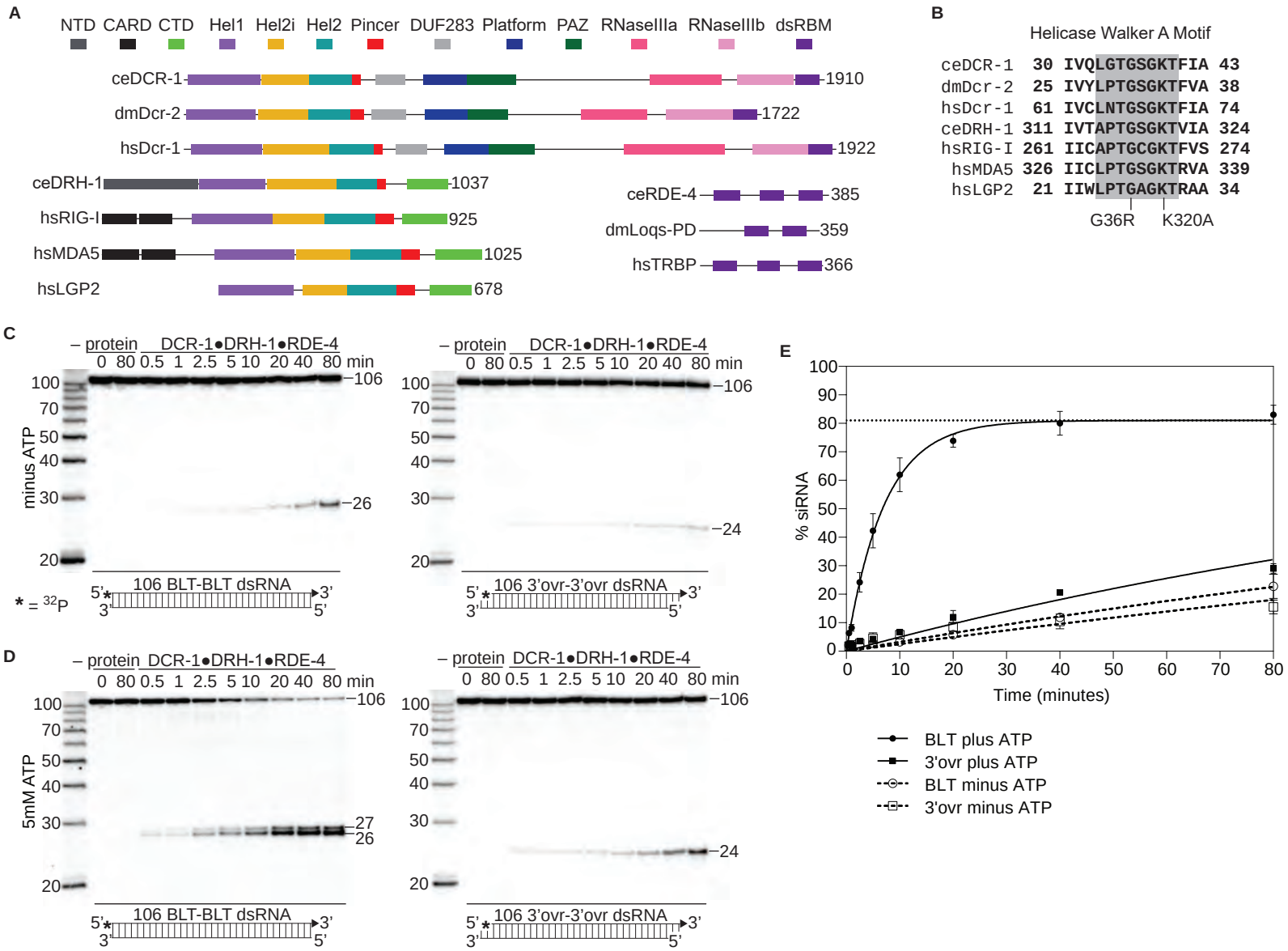

Figure 1. The *C. elegans* antiviral complex DCR-1•DRH-1•RDE-4 preferentially cleaves blunt dsRNA in an ATP-dependent manner.

A. Colored rectangles depict conserved domains. NCBI conserved domains[65], Clustal Omega Multiple Sequence Alignments[66–68], and previous reports[11,28,34] were used in defining domain boundaries. Numbers to right of open-reading frame indicate total amino acids in protein. Organism is indicated: ce, *C. elegans*; dm, *Drosophila melanogaster*, hs, *Homo sapiens*.

B. Amino acids within Walker A motif (shaded) of the Hel1 subdomain with mutations indicated for DCR-1 (G36R) and DRH-1 (K320A). Number indicates the residues at the beginning and end.

C. Single-turnover cleavage assays of DCR-1•DRH-1•RDE-4 (25nM) with 106 BLT or 3'ovr dsRNA (1nM) at 20°C in the absence of ATP. Sense (top) strand was 5' ^{32}P-end labeled (*) and contained a 2',3' cyclic phosphate (filled triangle in cartoon under gel) to minimize cleavage from that end (see Figure S2). Products were separated by 17% denaturing PAGE, and a representative PhosphorImage is shown (n ≥ 3). Left, marker nucleotide lengths. See also Figures S1 – S3.

D. Same as C except with 5mM ATP added to the reaction.

E. Quantification of single-turnover assays as in C and D with symbol key below. Data points are mean ± SD (n = 3). Dotted line indicates amplitude constraint (see Materials and methods).

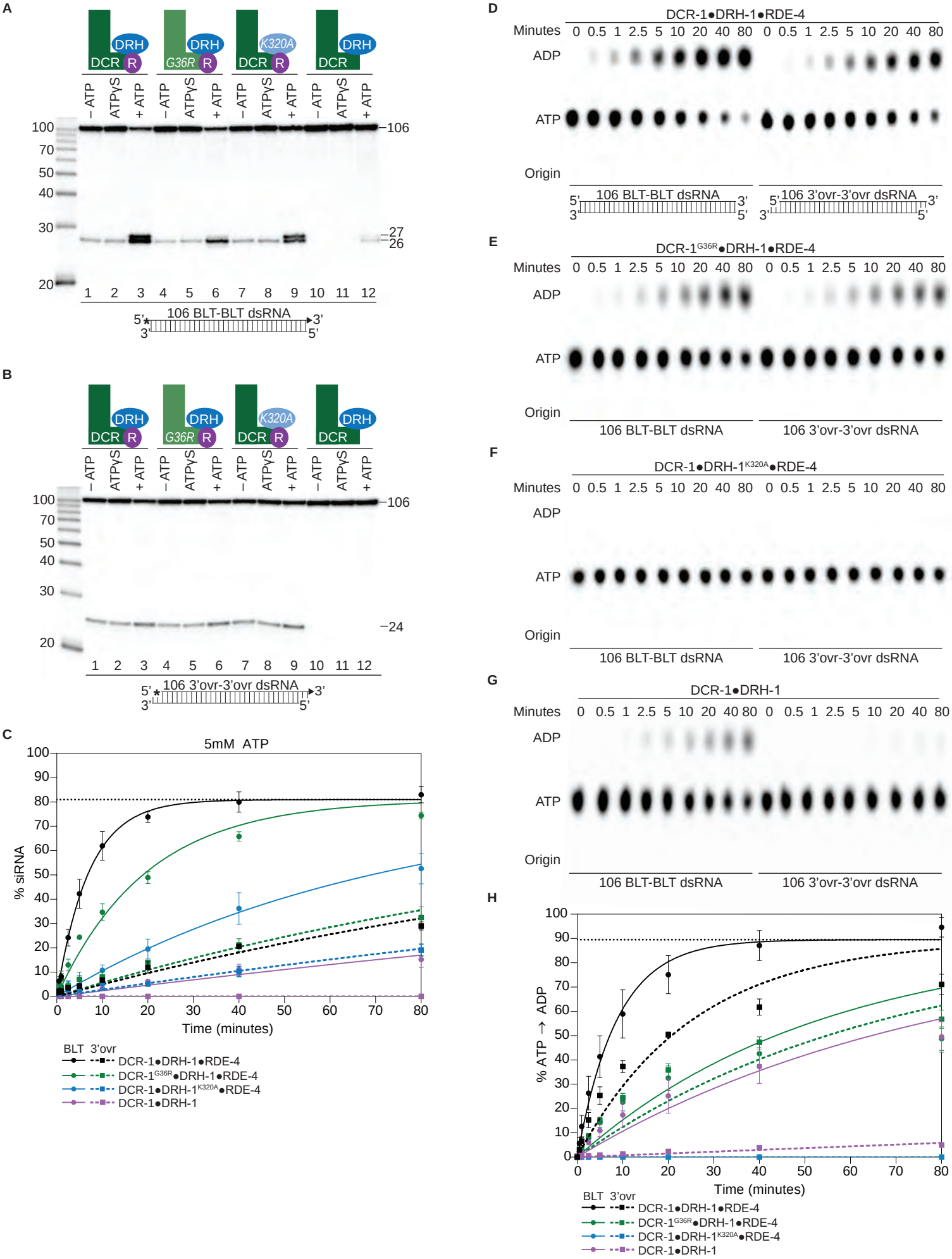
A
DRH
DCR
R
G36R
K320A
– ATP
ATPγS
+ ATP
100
70
50
40
30
20
106
27
26
1 2 3 4 5 6 7 8 9 10 11 12
106 BLT-BLT dsRNA
5'
3'
B
24
106 3'ovr-3'ovr dsRNA
C
5mM ATP
% siRNA
Time (minutes)
BLT 3'ovr
DCR-1●DRH-1●RDE-4
DCR-1G36R●DRH-1●RDE-4
DCR-1●DRH-1K320A●RDE-4
DCR-1●DRH-1
D
DCR-1●DRH-1●RDE-4
Minutes 0 0.5 1 2.5 5 10 20 40 80 0 0.5 1 2.5 5 10 20 40 80
ADP
ATP
Origin
106 BLT-BLT dsRNA
106 3'ovr-3'ovr dsRNA
E
DCR-1G36R●DRH-1●RDE-4
F
DCR-1●DRH-1K320A●RDE-4
G
DCR-1●DRH-1
H
% ATP → ADP

Figure 2. ATP-dependent cleavage reactions are mediated by DCR-1 and DRH-1 helicase domains, whereas RDE-4 is needed for ATP-independent and ATP-dependent cleavage reactions.

A. Single-turnover cleavage assays of 106 BLT dsRNA (1nM) with indicated protein complex (25nM) ± 5mM ATP or ATPγS, incubated at 20°C for 60 minutes. Sense strand was 5' ^{32}P-end labeled (*) and contained a 2',3' cyclic phosphate (filled triangle in cartoon under gel) to minimize cleavage from the opposite end (see Figure S2). Products were separated by 17% denaturing PAGE, and a representative PhosphorImage is shown (n = 3). Left, marker nucleotide lengths.

B. Same as A except with 106 3'ovr dsRNA (1nM).

C. Quantification of single-turnover assays over time, using wildtype or variant antiviral complexes as indicated (25nM), with 106 BLT dsRNA (1nM) or 106 3'ovr dsRNA (1nM) plus 5 mM ATP. Data points are mean ± SD (n = 3). See Figure S4A – S4C for representative primary data. Plateau constrained to 81.02 (dotted line). See Materials and methods.

D. DCR-1•DRH-1•RDE-4 (25nM) was incubated with 106 BLT or 3'ovr dsRNA (400nM) with 100μM α-^{32}P-ATP at 20°C. ATP hydrolysis monitored by thin-layer chromatography (TLC), and a representative PhosphorImage is shown (n ≥ 3). Positions of origin, ATP, and ADP are indicated. See also Figure S4D – S4E.

E – G. Same as D except with complexes indicated.

H. Quantification of ATP hydrolysis assays as in D – G. Data points are mean ± SD (n = 3) with symbol key below graph. Plateau constrained to 89.55 (dotted line). See Materials and methods.

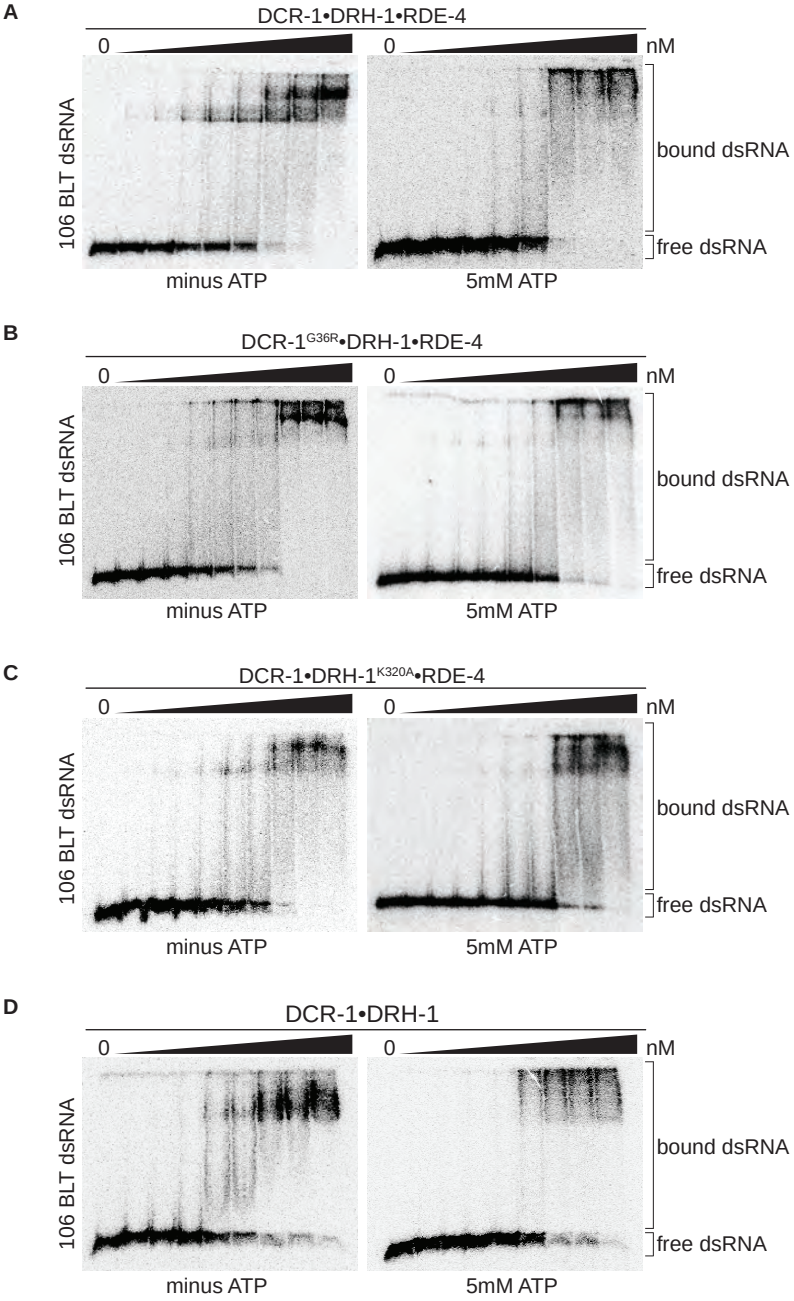
A
DCR-1•DRH-1•RDE-4
0
0
nM
106 BLT dsRNA
bound dsRNA
free dsRNA
minus ATP
5mM ATP
B
DCR-1G36R•DRH-1•RDE-4
0
0
nM
106 BLT dsRNA
bound dsRNA
free dsRNA
minus ATP
5mM ATP
C
DCR-1•DRH-1K320A•RDE-4
0
0
nM
106 BLT dsRNA
bound dsRNA
free dsRNA
minus ATP
5mM ATP
D
DCR-1•DRH-1
0
0
nM
106 BLT dsRNA
bound dsRNA
free dsRNA
minus ATP
5mM ATP

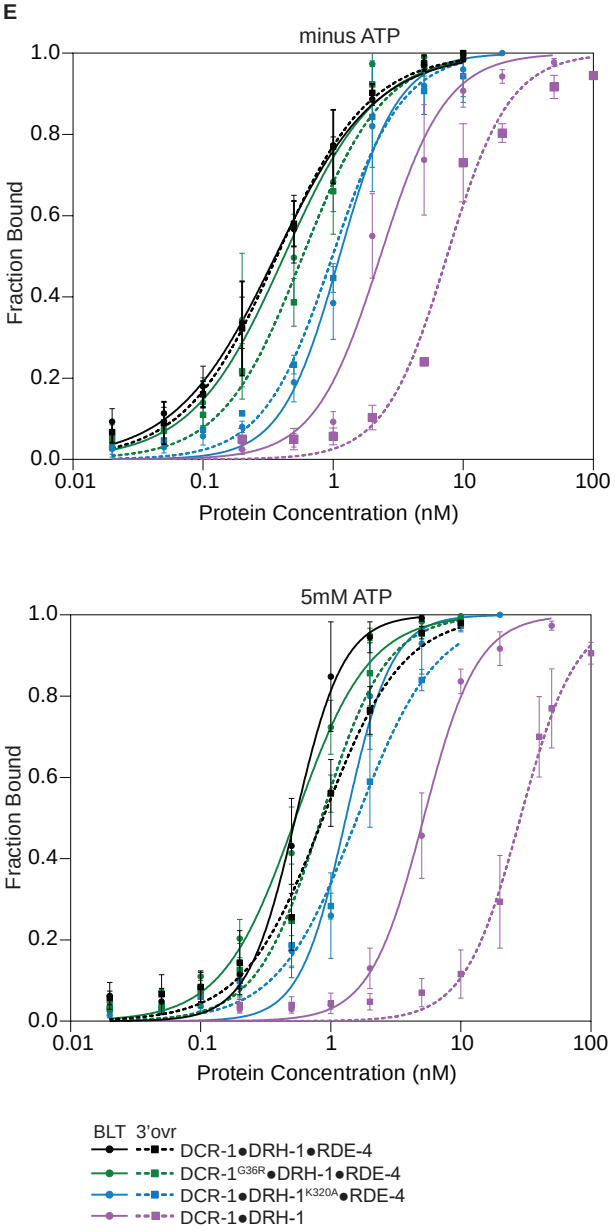
E
minus ATP
Fraction Bound
1.0
0.8
0.6
0.4
0.2
0.0
0.01
0.1
1
10
100
Protein Concentration (nM)
5mM ATP
Fraction Bound
1.0
0.8
0.6
0.4
0.2
0.0
0.01
0.1
1
10
100
Protein Concentration (nM)
BLT 3'ovr
DCR-1•DRH-1•RDE-4
DCR-1G36R•DRH-1•RDE-4
DCR-1•DRH-1K320A•RDE-4
DCR-1•DRH-1

Figure 3. Binding affinity of DCR-1•DRH-1•RDE-4 wildtype and mutant complexes for 106 BLT dsRNA in the absence or presence of ATP.

A. Representative PhosphorImages showing gel mobility shift assays with increasing concentrations ranging from 0 to 5nM of DCR-1•DRH-1•RDE-4 with 106 BLT dsRNA ± 5mM ATP as indicated. Sense strand was 5' ^{32}P-end labeled (*) and contained a 2',3' cyclic phosphate. As labeled on right, all dsRNA that migrated through the gel more slowly than $dsRNA_{free}$ was considered bound.

B – D. Same as A except with indicated complexes. Protein concentrations increased from left to right as indicated and range from 0 to 10nM (B and C), and 0 to 50nM (D).

E. Radioactivity in PhosphorImages as in A-D was quantified to generate binding isotherms for wildtype and mutant complexes ± 5mM ATP (see key). Fraction bound was determined using radioactivity for $dsRNA_{free}$ and $dsRNA_{bound}$. Data was fit to calculate dissociation constant, K_d, using the Hill formalism, where fraction bound = $1/(1 + (K_d^n/[P]^n))$. Data points, mean ± SD ($n \geq 3$). See also Figure S5.

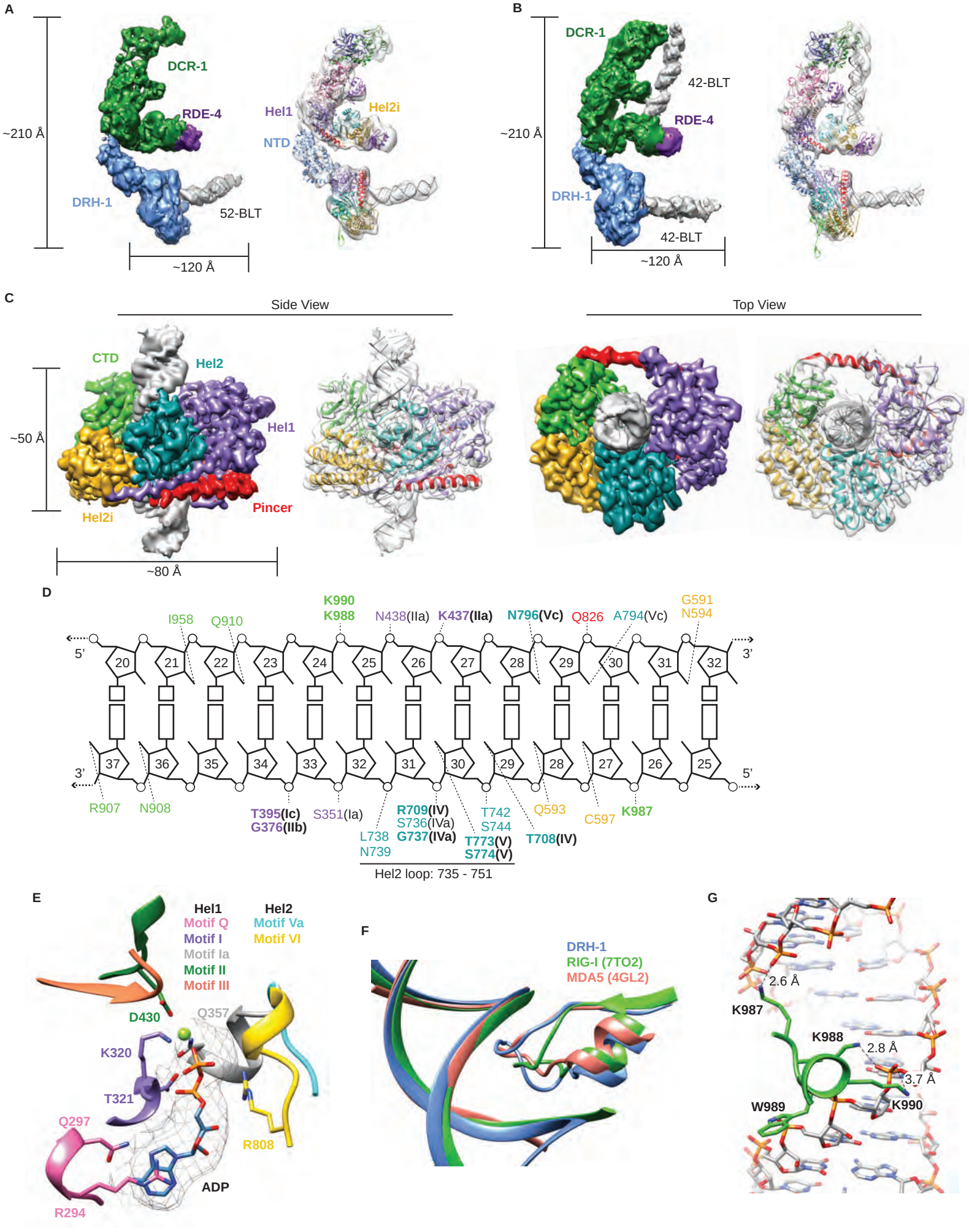
A
DCR-1
RDE-4
DRH-1
52-BLT
~210 Å
~120 Å
Hel1
Hel2i
NTD
B
DCR-1
42-BLT
RDE-4
DRH-1
42-BLT
~210 Å
~120 Å
C
Side View
Top View
CTD
Hel2
Hel1
Hel2i
Pincer
~50 Å
~80 Å
D
5'
3'
K990
K988
I958
Q910
N438(IIa)
K437(IIa)
N796(Vc)
Q826
A794(Vc)
G591
N594
20
21
22
23
24
25
26
27
28
29
30
31
32
37
36
35
34
33
32
31
30
29
28
27
26
25
R907
N908
T395(Ic)
G376(IIb)
S351(Ia)
L738
N739
R709(IV)
S736(IVa)
G737(IVa)
T742
S744
T773(V)
S774(V)
T708(IV)
Q593
C597
K987
Hel2 loop: 735 - 751
E
Hel1
Motif Q
Motif I
Motif Ia
Motif II
Motif III
Hel2
Motif Va
Motif VI
D430
Q357
K320
T321
Q297
R808
ADP
R294
F
DRH-1
RIG-I (7TO2)
MDA5 (4GL2)
G
2.6 Å
K987
K988
2.8 Å
3.7 Å
W989
K990

Figure 4. Cryo-EM analyses provide insight into ATP-dependent and ATP-independent cleavage mechanisms.

A. 6.1 Å reconstruction of DCR-1•DRH-1•RDE-4. DCR-1 and RDE-4 densities were fitted with human Dicer in complex with TRBP (PBD 5ZAK)[40], DRH-1 density was fitted with an AlphaFold2 model of DRH-1[44,45], and a 52-BLT A-form dsRNA was built in Chimera[69]. Color of protein names correlates with model colors. See also Figure S7.

B. 7.6 Å reconstruction of DCR-1•DRH-1•RDE-4. DCR-1 and RDE-4 densities were fit with PBD 5ZAL[40], DRH-1 density was fit with the AlphaFold2 prediction of DRH-1[44,45], and a 42-BLT A-form dsRNA was built in Chimera[69]. See also Figure S8.

C. 3D reconstruction at 2.9 Å fitted with a refined model of the helicase and CTD domains of DRH-1 and dsRNA. See also Figure S9 and Table S2.

D. The interactions between DRH-1 and dsRNA, determined with a 3.7 Å cutoff for contacts. Bold residues indicate residues that are identical with RIG-I, MDA5, or both. See also Figure S10.

E. ADP, Mg^{++}, and surrounding helicase motifs. Colors: motif Q (pink), motif I (purple), motif Ia (gray), motif II (green), motif III (coral), motif Va (cyan), and motif VI (yellow). The density of ADP is shown in mesh.

F. Conserved loop in the Hel2 domain is inserted into the dsRNA major groove. DRH-1 = blue, residues 733 – 756; RIG-I (7TO2) = green, residues 659 – 679; MDA5 (4GL2) = salmon, residues 752 – 773. Note that this figure includes residues on each side of the loop. See also Figure S10.

G. Lysines 987, 988, and 990 interact with the dsRNA backbone. See also Figure S10.

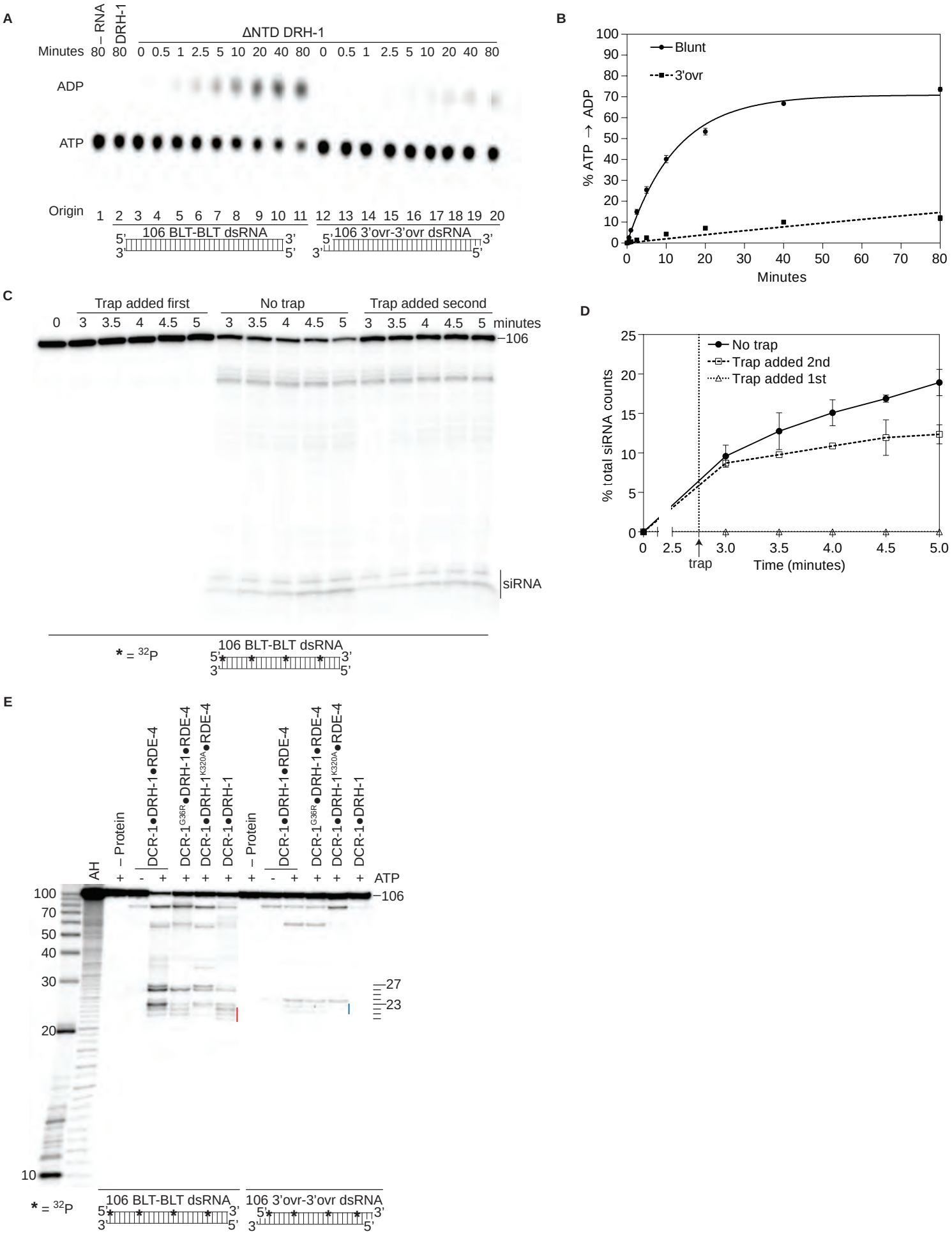
A
– RNA
DRH-1
ΔNTD DRH-1
Minutes 80 80 0 0.5 1 2.5 5 10 20 40 80 0 0.5 1 2.5 5 10 20 40 80
ADP
ATP
Origin 1 2 3 4 5 6 7 8 9 10 11 12 13 14 15 16 17 18 19 20
106 BLT-BLT dsRNA
106 3'ovr-3'ovr dsRNA
B
Blunt
3'ovr
% ATP → ADP
Minutes
C
Trap added first
No trap
Trap added second
0 3 3.5 4 4.5 5 3 3.5 4 4.5 5 3 3.5 4 4.5 5 minutes
–106
siRNA
106 BLT-BLT dsRNA
* = 32P
D
No trap
Trap added 2nd
Trap added 1st
% total siRNA counts
trap
Time (minutes)
E
AH
– Protein
DCR-1●DRH-1●RDE-4
DCR-1G36R●DRH-1●RDE-4
DCR-1●DRH-1K320A●RDE-4
DCR-1●DRH-1
ATP
–106
27
23
106 BLT-BLT dsRNA
106 3'ovr-3'ovr dsRNA
* = 32P

Figure 5. Autoinhibition of DRH-1 is relieved to promote processive cleavage.

A. Full length DRH-1 (25nM) was incubated with 106 BLT dsRNA (400nM) with 100μM α-^{32}P-ATP at 20°C (lane 2). ΔNTD DRH-1 (25nM) was incubated without RNA (-RNA; lane 1) or with 400nM 106 BLT (lanes 3 – 11) or 3'ovr dsRNA (lanes 12 – 20) with 100μM α-^{32}P-ATP at 20°C. ATP hydrolysis was monitored by TLC, and a representative PhosphorImage is shown. Positions of origin, ATP, and ADP are indicated.

B. Quantification of ATP hydrolysis assay as in A. Data points are mean ± SD (n = 3) with symbol key in graph. Plateau constrained to 89.55 (dotted line). See Materials and methods.

C and D. A representative PhosphorImage (C) shows trap experiments using 50nM DCR-1•DRH-1•RDE-4 and 1nM ^{32}P-internally-labeled 106 BLT dsRNA ± 2000nM 52 BLT cold dsRNA. Quantification (D) shows mean ± SD (n = 3). Cold dsRNA was added at 2.75 minutes as indicated by the vertical dotted line and arrow.

E. Single-turnover cleavage assays of 106 BLT or 106 3'ovr dsRNA (1nM) with indicated protein complex (25nM) ± 5mM ATP as indicated. Sense strand was ^{32}P-internally labeled to allow visualization of intermediates, with red line noting internal cleavage products of 21 – 23 nts and blue line noting 22 – 23 nt products. Products were separated by 17% denaturing PAGE, and a representative PhosphorImage is shown (n = 3). Left, marker nucleotide lengths. AH, alkaline hydrolysis.

A

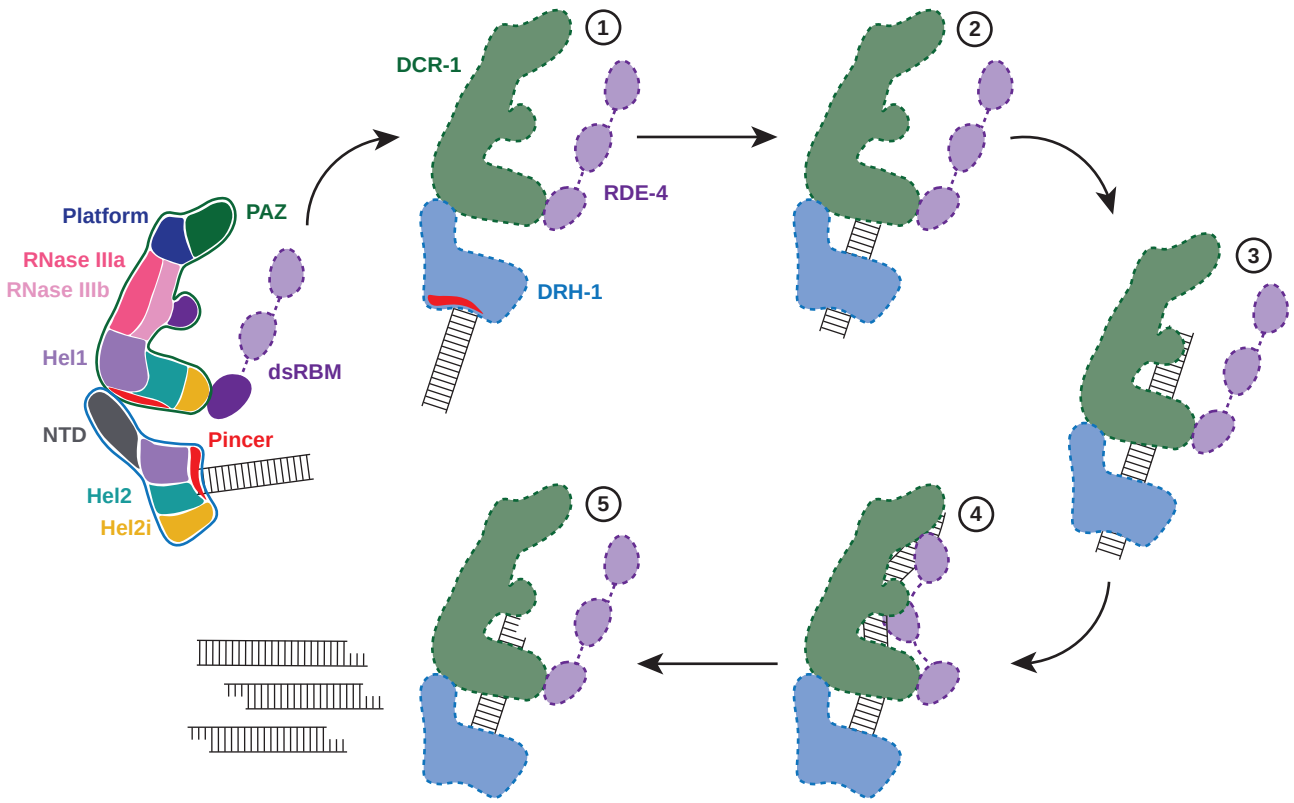
DCR-1
RDE-4
DRH-1
Platform
PAZ
RNase IIIa
RNase IIIb
Hel1
dsRBM
NTD
Pincer
Hel2
Hel2i
1
2
3
4
5

B

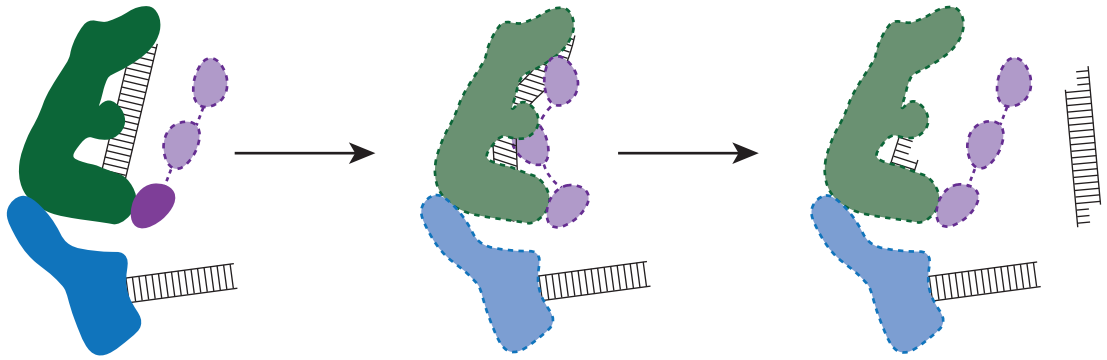

Figure 6. Working model of dsRNA cleavage by DCR-1•DRH-1•RDE-4.

A. Model for ATP-dependent cleavage. Far left shows cartoon of complex with domains color-coded. Illustrations 1-5 show proposed steps as discussed in text, with DCR-1 (green), DRH-1, (blue) and RDE-4 (purple). Solid lines indicate structures observed in our cryo-EM studies, while dashed lines indicate proposed intermediates not yet observed. Pincer subdomain (red) is colored to orient proposed DRH-1 conformational change. Additional details in text.

B. Model for ATP-independent cleavage, with colors and solid and dashed lines as in A.

Table 1. Summary of k_{obs}, $t_{1/2}$, and K_d values					
	k_{obs} (min^{-1}) (Cleavage)	$t_{1/2}$ (min) (Cleavage)	k_{obs} (min^{-1}) (ATP Hydrolysis)	K_d (nM)	
	+ ATP	+ ATP	+ ATP	- ATP	+ ATP
DCR-1•DRH-1•RDE-4					
106 BLT	0.14 ± 0.01	4.9	0.11 ± 0.01	0.30 ± 0.04	0.53 ± 0.04
106 3'ovr	0.006 ± 0.0005	109.6	0.03 ± 0.005	0.37 ± 0.04	0.87 ± 0.10
DCR-1^{G36R}•DRH-1•RDE-4					
106 BLT	0.05 ± 0.004	13.65	0.018 ± 0.002	0.42 ± 0.06	0.53 ± 0.05
106 3'ovr	0.007 ± 0.0007	95.99	0.014 ± 0.002	0.58 ± 0.07	0.85 ± 0.08
DCR-1•DRH-1^{K320A}•RDE-4					
106 BLT	0.013 ± 0.001	49.77	n.d.	1.12 ± 0.12	1.31 ± 0.13
106 3'ovr	0.003 ± 0.0004	199.6	n.d.	0.99 ± 0.10	1.60 ± 0.15
DCR-1•DRH-1					
106 BLT	0.002 ± 0.0003	235.2	0.012 ± 0.001	2.11 ± 0.28	5.18 ± 0.33
106 3'ovr	n.d.	n.d.	n.d.	7.50 ± 0.80	28.64 ± 2.03
ΔNTD DRH-1					
106 BLT			0.08		
106 3'ovr			0.002		

Values shown are mean ± SD (n = 3). n.d., not detected.